

Properties of $z \sim 3\text{--}6$ Lyman break galaxies. II. Testing star formation histories and the SFR–mass relation with ALMA and near-IR spectroscopy

D. Schaerer^{1,2}, S. de Barros¹, P. Sklias¹

¹ Observatoire de Genève, Université de Genève, 51 Ch. des Maillettes, 1290 Versoix, Switzerland

² CNRS, IRAP, 14 Avenue E. Belin, 31400 Toulouse, France

Received date; accepted date

ABSTRACT

Context. Understanding the relation between the star formation rate (SFR) and stellar mass (M_*) of galaxies, and the evolution of the specific star formation rate ($sSFR=SFR/M_*$).

Aims. We examine the dependence of derived physical parameters of distant Lyman break galaxies (LBGs) on the assumed star formation histories (SFHs), their implications on the SFR–mass relation, and we propose observational tests to better constrain these quantities.

Methods. We use our SED-fitting tool including nebular emission to analyze a large sample of LBGs from redshift $z \sim 3$ to 6, assuming five different star formation histories, extending our first analysis of this sample (de Barros et al. 2012, paper I). In addition we predict the IR luminosities consistently with the SED fits.

Results. Compared to “standard” SED fits assuming constant SFR and neglecting nebular lines, assuming variable SFHs yield systematically lower stellar masses, higher extinction, higher SFR, higher IR luminosities, and a wider range of equivalent widths for optical emission lines. Exponentially declining and delayed SFHs yield basically identical results and generally fit best. Exponentially rising SFHs yield similar masses, but somewhat higher extinction than exponentially declining ones. We find significant deviations between the derived SFR and IR luminosity from the commonly used SFR(IR) or SFR(IR+UV) calibration, due to differences in the SFHs and ages. Models with variable SFHs, favored statistically, yield generally a large scatter in the SFR–mass relation. We show the dependence of this scatter on assumptions of the SFH, the introduction of an age prior, and on the extinction law. We show that the true scatter in the SFR–mass relation can be significantly larger than inferred using SFR(UV) and/or SFR(IR), if the true star formation histories are variable and relatively young populations are present. Different SFHs, and hence differences in the derived SFR–mass relation and in the specific star formation rates, can be tested/constrained observationally with future IR observations with ALMA. Measurement of emission lines, such as $H\alpha$ and $[O\text{ II}]\lambda 3727$, can also provide useful constraints on the SED models, and hence test the predicted physical parameters.

Conclusions. Our findings of a large scatter in the SFR–mass relation at high- z and an increase of the specific star formation rate above $z \gtrsim 3$ (paper I) can be tested observationally. Consistent analysis of all observables including the rest-frame UV to IR and emission lines are required to establish more precisely true SFR values and the scatter in the SFR–mass relation.

Key words. Galaxies: starburst – Galaxies: ISM – Galaxies: high-redshift – Ultraviolet: galaxies – Radiative transfer

1. Introduction

One of the important, recent results of multi-wavelength galaxy surveys is the finding of a well-defined relation between the star formation rate (SFR) and stellar mass of galaxies – now often called the main sequence of star forming galaxies – and the evolution of this relation with redshift, at least from the nearby Universe up to redshift $z \sim 2$ (Noeske et al. 2007; Daddi et al. 2007; Elbaz et al. 2007; Rodighiero et al. 2011). The observed redshift evolution corresponds to an increase of the typical specific star formation rate ($sSFR$) by more than an order of magnitude from $z \sim 0$ to 2, indicating a higher star formation activity of galaxies in the past.

Recent analysis of Lyman break galaxies (LBGs), combining often HST and Spitzer observations, have tried to examine whether a SFR–mass relation is already in place at higher redshift, and how the specific star formation rate of galaxies behaves at $z \sim 4\text{--}7$ (e.g. Stark et al. 2009; Schaerer & de Barros 2010; Labbé et al. 2010; McLure et al. 2011; González et al. 2011). The first studies have found a relation similar to the $z \sim 2$

SFR–mass relation, which would indicate no evolution of the $sSFR$ beyond redshift $z \gtrsim 2$ – a plateau in $sSFR$ – (e.g. Stark et al. 2009; González et al. 2011). This result appears difficult to reconcile with most theoretical models, which successfully explain the behavior of star formation properties from $z \sim 0$ to 2, but predict a continuing rise of the specific star formation rate towards higher redshift (Bouché et al. 2010; Dutton et al. 2010; Weinmann et al. 2011; Davé et al. 2011), although others propose alternatives (Krumholz & Dekel 2012, e.g.). More recent work, including different spectral energy distribution (SED) models, or allowing for a revision of dust attenuation have shown that the observed $sSFR$ at $z \sim 5\text{--}7$ could be higher than previously thought (Schaerer & de Barros 2010; de Barros et al. 2011; Bouwens et al. 2011; Yabe et al. 2009; de Barros et al. 2012).

If all galaxies at $z \gtrsim 2$ obey a mass–SFR relation with star formation rate increasing with galaxy mass, it is evident that their star formation rate must increase with time. The apparent, small scatter in the SFR–mass relation, and the value of

the exponent α close to unity in this relation $\text{SFR} \propto M_*^\alpha$ found by various studies (e.g. Daddi et al. 2007; Elbaz et al. 2007; González et al. 2011) has led several authors to conclude that high redshift galaxies must have gone through a phase of quasi-exponential growth (e.g. Renzini 2009; Maraston et al. 2010). Earlier studies have independently advocated rising star formation histories (SFHs) for high redshift galaxies from hydrodynamic simulations and semi-analytical models (Finlator et al. 2007, 2010; Lee et al. 2010; Finlator et al. 2011). Arguments in favor of rising SFHs, at least on average, have been put forward by Finkelstein et al. (2010); Papovich et al. (2011) to explain the evolution of the UV luminosity function. If representative of the star formation history of individual galaxies, such star formation histories would indeed be quite different from exponentially declining or constant SFHs, most frequently assumed in the literature to model/analyze the observed SED of distant galaxies.

Assumptions on the star formation history affect the physical parameters of galaxies derived from SED fits. This is therefore generally treated as a free parameter. See e.g. Reddy et al. (2010); Maraston et al. (2010); Wuyts et al. (2011); Reddy et al. (2012) for examples on $z \gtrsim 2$ star forming galaxies. Determining star formation histories and their associated timescales is also important, as this may provide constraints on different modes of star formation and on feedback processes at high redshift, recognized as key features for our understanding of galaxy evolution. For example, star formation may proceed on different timescales if regulated by cold-accretion or by star formation feedback or triggered by mergers (cf. Khochfar & Silk 2011; Wyithe & Loeb 2011). These points already illustrate the interest and importance of determining the star formation histories and typical timescales of star formation at high z . We here wish to discuss and reexamine these issues on the basis of an analysis of a large sample of LBGs covering redshifts from ~ 3 to 6, and to present observational tests which should be able to distinguish different star formation histories.

One of main arguments often invoked to argue for rising star formation histories is the small scatter of the SFR–mass relation. However, it should be recognized that generally the SFR is derived from observables – the UV or IR luminosity – which depend on relatively long ($\gtrsim 100$ Myr) timescales, and which are assumed to be at an equilibrium value, which is only reached after this timescale and for constant SFR. With these assumptions entering e.g. the commonly used SFR(UV) or SFR(IR) calibrations or Kennicutt (1998), it is natural that the “observational” scatter is smaller than the true scatter in the current SFR, if typical ages are less than 100 Myr and/or the timescale shorter than this. Especially at high redshift, where timescales are shorter (e.g. the dynamical timescale decreases with $(1+z)^{-3/2}$, cf. Wyithe & Loeb 2011) one should therefore carefully (re)examine the SFR–mass relation and its “tightness” using consistent diagnostics, and with all the available observational constraints including on age, star formation timescales and histories. In any case, the conclusion that rising SFHs are favored is *a priori* inconsistent with the assumptions leading to it. Although this has been re-examined for $z \sim 2$ samples (Maraston et al. 2010; Wuyts et al. 2011; Reddy et al. 2012) this obviously calls for a revision at higher redshifts.

Most SED studies of LBGs at $z \gtrsim 3$ have assumed constant star formation rates, or exponentially declining SFHs to determine the physical parameters of these galaxies (e.g. Egami et al. 2005; Schaerer & Pelló 2005; Eyles et al. 2005; Verma et al. 2007; Yabe et al. 2009; Stark et al. 2009; Lee et al. 2010; Schaerer & de Barros 2010; González et al. 2011), some of them imposing no dust attenuation, motivated by the blue UV

slopes observed at high redshift. Notable examples are the work of Finlator et al. (2007) who analyzed 6 galaxies at $z > 5.5$ with different SFHs, including rising ones taken from their hydrodynamic simulations. The physical parameters they derive are consistent with those using simple parametrised histories, albeit with reduced uncertainties. Their study also shows that SED fits with rising star formation histories yield a higher attenuation than inferred assuming constant SFR, a result not yet appreciated enough, which we also find in de Barros et al. (2012) and in this paper.

Another drawback of most earlier studies is that the contribution of nebular emission (most emission lines) is not taken into account, an effect which can significantly alter the ages, masses, and other physical parameters derived from SED fits, as demonstrated by Schaerer & de Barros (2009, 2010). Indeed, there is now clear evidence for the presence of nebular lines affecting the broad-band photometry of high- z star-forming galaxies (Lyman alpha emitters and LBGs in particular), as discussed e.g. in Schaerer & de Barros (2011). The best demonstration comes from LBGs with spectroscopic redshifts between 3.8 and 5, among which a large fraction shows a clear excess in the $3.6 \mu\text{m}$ filter with respect to neighboring filters (K and $4.5 \mu\text{m}$), as shown by Shim et al. (2011a). At these redshifts $\text{H}\alpha$ is located in the $3.6 \mu\text{m}$ filter, whereas very few lines are expected at $4.5 \mu\text{m}$, showing that the observed $3.6 \mu\text{m}$ excess is naturally explained by strong $\text{H}\alpha$ emission.

Given these limitations of published SED studies and the interesting results obtained from our work on a small sample of $z \sim 6$ –8 LBGs (Schaerer & de Barros 2010), we have recently undertaken an extensive study of the physical parameters of a large sample of ~ 1400 LBGs at $z \sim 3$ –6, using our state-of-the-art photometric redshift and SED fitting model including nebular emission, and considering a range of different star formation histories. Among the numerous detailed results obtained in this work (de Barros et al. 2012, hereafter dBSS12) we find in particular on the preferred models: 1) a large scatter in the SFR–mass relation for the preferred, variable star formation histories, 2) higher dust attenuation than obtained from models assuming $\text{SFR}=\text{const}$ and from standard methods using the UV slope, and 3) a higher sSFR than commonly obtained, and a rising sSFR with redshift. Our models therefore reconcile the observationally-inferred specific star formation rate with predictions from cosmological models predicting a continuous rise of the sSFR with redshift (Bouché et al. 2010; Dutton et al. 2010; Weinmann et al. 2011; Davé et al. 2011; Krumholz & Dekel 2012). The results from dBSS12 have also other important implications, e.g. on the typical star formation timescales at high redshift, and on the cosmic star formation rate density.

Given the importance of these findings, it is of interest to carry out additional independent tests of the models and to provide further constraints on the ages, extinction, and star formation histories of high redshift galaxies. In this paper we present predictions allowing such tests. Furthermore, we extend the study of dBSS12 by exploring other star formation histories, not considered in our previous paper. Indeed, while dBSS12 adopted the fixed, rising star history of Finlator et al. (2011) obtained from the hydrodynamic simulations, we here explore exponentially rising SFHs and so-called “delayed” histories with variable timescales. These histories were previously applied to the SED fits of galaxies at lower redshift, e.g. at $z \sim 2$ by Maraston et al. (2010); Wuyts et al. (2011); Reddy et al. (2012) and found to be preferred over other simple star formation histories.

First, we examine the effect of the different SFHs on the derived physical parameters of LBGs. We then present the implications these different model assumptions have on the SFR–mass relation. After that we present consistent predictions for the infrared luminosity of these galaxies, based on their SED fits and the assumption of energy conservation, abandoning the standard SFR– L_{IR} conversions. We show in particular that such a consistent prediction yields a smaller scatter in the observables (L_{IR}) than in the current SFR. The true star formation rate of LBGs at $z \gtrsim 3$ could thus very well show a large scatter around a “main sequence” even if the UV and/or IR luminosities show a small scatter. Our models also show that star formation histories can, to some extent, be distinguished from measurement of IR luminosities, which will become possible with ALMA, since different amounts of UV attenuation are expected for different SFHs. We also present the predicted strength of some selected emission lines, which can be used to test our models and the different star formation histories.

Our paper is structured as follows. The observational data and the method used for SED modelling are described in Sect. 2. The dependence of the physical parameters on the assumed star formation histories is discussed in Sect. 3. Our general predictions for the IR emission are presented in Sect. 4. Specific predictions for $z \sim 4 - 6$ LBGs and ALMA are given in Sect. 5. The predicted strengths of optical emission lines are shown in Sect. 6. We discuss our results in Sect. 7, and Sect. 8 summarises our main conclusions. We adopt a Λ -CDM cosmological model with $H_0 = 70 \text{ km s}^{-1} \text{ Mpc}^{-1}$, $\Omega_m = 0.3$ and $\Omega_\Lambda = 0.7$.

2. Observational data and SED modelling

de Barros et al. (2012, hereafter dBSS12) have analysed a large sample of $z \sim 3-6$ dropout-selected galaxies in depth using an up-to-date photometric redshift and SED-fitting tool, that treats the effects of nebular emission on the SEDs of galaxies. In their homogeneous analysis they determine the main physical properties, such as the star formation rate (SFR), stellar mass, age, and reddening. They assess carefully their uncertainties, and discuss the evolution of these properties with redshift. We here extend these simulations to include other star formation histories and we examine the predicted IR luminosities and equivalent widths of selected emission lines from these galaxies.

2.1. Photometric data and sample selection

We have used the GOODS-MUSIC catalogue of Santini et al. (2009), which provide photometry in the U, B₄₃₅, V₆₀₆, i₇₇₆, z_{850LP}, J, H, and K bands mostly from the VLT and HST, and the 3.6, 4.5, 5.8, and 8.0 μm bands from the IRAC camera onboard *Spitzer*. Using standard criteria as in Nonino et al. (2009) and Stark et al. (2009) we then selected U, B, V, and i-drop galaxies. To reduce the contamination rate (typically $\sim 10-20\%$) we only retained the objects whose median photometric redshifts agree with the targetted redshift range. This leaves us with a sample of 389, 705, 199, and 60 galaxies with median photometric redshifts of $z_{\text{phot}} = 3.3, 3.9, 4.9$, and 6.0. See dBSS12 for more details.

2.2. SED models

Our SED-fitting tool, described in Schaerer & de Barros (2009) and Schaerer & de Barros (2010), is based on a version of the *Hyperz* photometric redshift code of Bolzonella et al. (2000),

modified to take nebular emission into account. In dBSS12 we considered a large set of spectral templates based on the GALAXEV synthesis models of Bruzual & Charlot (2003) and covering different metallicities and a wide range of star formation histories. A Salpeter IMF from 0.1 to 100 M_\odot was adopted. Our results can easily be rescaled to other IMFs with the same power law slope at high masses. Nebular emission from continuum processes and numerous emission lines were added to the spectra predicted from the GALAXEV models as described in Schaerer & de Barros (2009), proportionally to the Lyman continuum photon production. Following the results of dBSS12 we set the Ly α line to zero for $z \sim 3-5$, and we assume the case B value for the i-drop sample. The intergalactic medium (IGM) was treated with the prescription of Madau (1995).

The free parameters of our SED fits are: redshift z , metallicity Z (of stars and gas), the age t_\star defined since the onset of star-formation, and attenuation A_V described by the Calzetti law (Calzetti et al. 2000). For comparison, a subsample of the data was also modeled using the SMC extinction law (cf. Sect. 7).

Since one of the main objectives of this paper is to explore a variety of star formation histories (SFHs), we have adopted five different histories, which are summarized in Table 1, and illustrated in Fig. 1. Note that for exponentially rising SFHs the SFR is set to zero, after a growth by more than 20 decades. The bolometric luminosity output per unit SFR, respectively its inverse SFR/ L_{bol} , and the mass-to-light ratio in the V-band corresponding to these simple star formation histories are shown in Figs. 2 and 3. The behavior of these quantities are fundamental to explain the main differences in star formation rate and stellar mass obtained from different models, discussed in Sect. 3.

The first three cases, constant star formation, exponentially declining SF, and the average rising SFH predicted by the hydrodynamical models of Finlator et al. (2011) have already been used by de Barros et al. (2012). Two additional SFHs, exponentially rising, and so-called “delayed” SF showing a initial increase and subsequent decrease of the star formation, are also considered here. The way these assumed SFHs modify the derived physical parameters of LBGs and how they could be distinguished is discussed below.

Table 1. Star formation histories modeled in this work. All describe the evolution of the SFR with time (age t). Three of them have one additional free parameter, the SF timescale τ . For model B a minimum age of 50 Myr is assumed, for comparison with other studies. Models A, B, and C are the same as in dBSS12. The color code used in the figures is indicated in the last column.

ID	SF history	functional form	parameters	color
A=DEC	exp. declining	$\text{SFR} \propto \exp^{-t/\tau}$	t, τ	green
B=REF	constant	$\text{SFR} = \text{const}$	$t \geq 50 \text{ Myr}$	black
C=RIS	rising	Finlator+2011	t	blue
D	exp. rising	$\text{SFR} \propto \exp^{+t/\tau}$	t, τ	red
E	delayed	$\text{SFR} \propto t \exp^{-t/\tau}$	t, τ	yellow

In practice we compute for each model set (i.e. star formation history) SED fits for all combinations of $z \in [0, 10]$ in steps of 0.1 $Z = (0.02=Z_\odot, 0.004, 0.001)$, $\tau = (0.01, 0.03, 0.05, 0.07,$

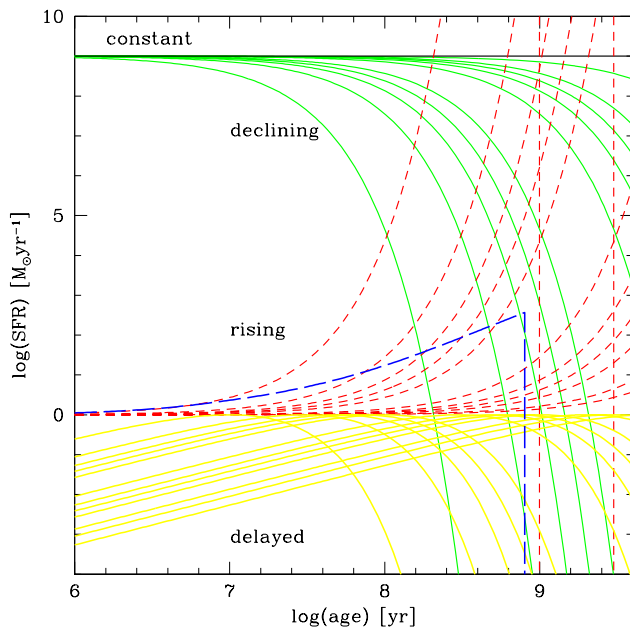


Fig. 1. Illustration of the star formation histories adopted in this paper. Shown is the SFR as a function of age. Within each model set A–E the curves are normalized to an arbitrary value. The colors used for the different SFHs are listed in Table 1.

0.1, 0.3, 0.5, 0.7, 1., 3., ∞) Gyr for model A¹, 51 age steps from 0 to the age of the Universe (see Bolzonella et al. 2000), $A_V \in [0, 2]$ mag in steps of 0.05. Minimisation over the entire parameter space yields the best-fit parameters and SED, along with other properties such as the stellar mass and star formation rate (SFR) and UV magnitude. Other physical parameters, briefly described below, are determined from the best-fit SED. To determine the uncertainties of the physical parameters, we used Monte-Carlo simulations by running 1000 realisations of each object. From this we derived the probability distribution function for each parameter/quantity, either for each individual object or for (sub)samples.

2.3. Predicted physical parameters and observables

In addition to the fit parameters of our models, redshift z , metallicity Z , age t , SF timescale τ , stellar mass M_* , and current star formation rate SFR, our models also allow us to determine other parameters and observables of interest. We briefly describe them here, for sake of clarity. Note that for all the physical parameters and observables we determine the detailed probability distribution function (pdf) from the full MC simulations. From the 1D pdf we derive in particular the median value and the 68% confidence interval, which we use to illustrate the uncertainties on these parameters. For most of the paper we use for simplicity the median value of the physical parameter of interest.

2.3.1. Emission lines

From the numerous emission lines included in our spectral templates we select some lines, primarily Ly α , H α , H β , [O II] $\lambda 3727$,

¹ For exponentially rising SFHs we explore $\tau = (0.01, 0.03, 0.05, 0.07, 0.1, 0.3, 0.5, 0.7, 1., 2., 3.)$ Gyr, for delayed histories $\tau = (0.01, 0.03, 0.05, 0.07, 0.1, 0.3, 0.5, 0.7, 1., 2., 3., 4., 5.)$ Gyr.

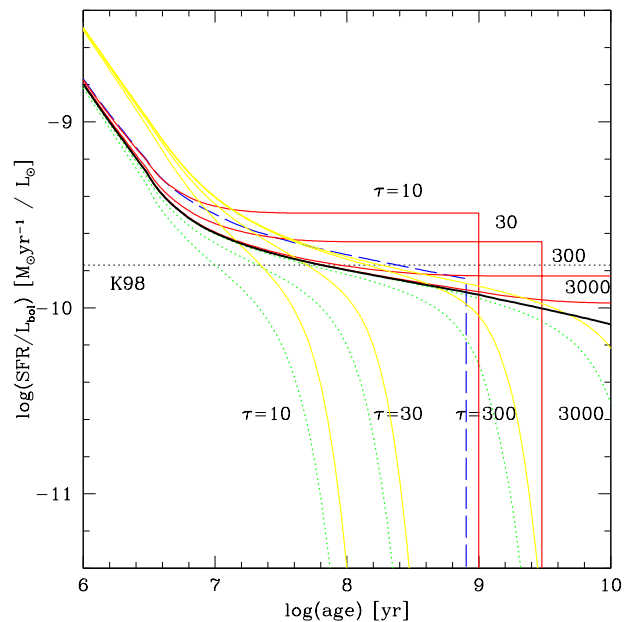


Fig. 2. Predicted ratio SFR/ L_{bol} as function of time for the some of the models with exponentially decreasing, delayed, and exponentially rising SFHs (with timescales $\tau = 10, 30, 300, 3000$ Myr indicated), compared to the case of constant SFR. The plots are shown here for BC2003 models with solar metallicity. Same color codes as in Fig. 1. The standard SFR(IR) conversion factor from Kennicutt (1998) is shown by the black dotted line.

[O II] $\lambda\lambda 4959, 5007$, for which we save the emission line fluxes and equivalent widths predicted by the photometric SED fits. These lines can subsequently be used for comparison with spectroscopic observations (existing or future).

2.3.2. UV and IR emission

For straightforward comparison with observations we use the absolute UV magnitude M_{1500} defined at 1500 Å, and derived from the SED using a square filter of 300 Å width centered on this wavelength.

To define an emergent (observed) UV luminosity L_{UV} we follow common practice by computing $L_{\text{UV}} = \lambda F_\lambda$, where $\lambda = 1800$ Å, and F_λ is the average flux between 1400 and 2200 Å. Assuming energy conservation, i.e. that the attenuated/extinct UV light is reemitted by dust in the IR, we can predict the amount of IR radiation expected from each galaxy. The corresponding IR luminosity L_{IR} is simply computed from the difference between the intrinsic, unattenuated SED, and the best-fit SED with the parameters. In practice L_{IR} is calculated from the attenuated energy integrated from 913 Å to 3 μm (cf. da Cunha et al. 2008; Noll et al. 2009). This quantity also includes the nebular emission (lines and continuum) if present in the SED, consistently with our assumption of identical attenuation for both stars and gas. We have checked that the integral over the Balmer continuum and up to 3 μm yield basically identical results.

From the UV and IR luminosity just defined, we also compute $L_{\text{IR+UV}}$, the emergent luminosity in the UV + IR domain, which is a good proxy of the total bolometric luminosity and to some extent also of the SFR (but cf. below). Similarly, we will

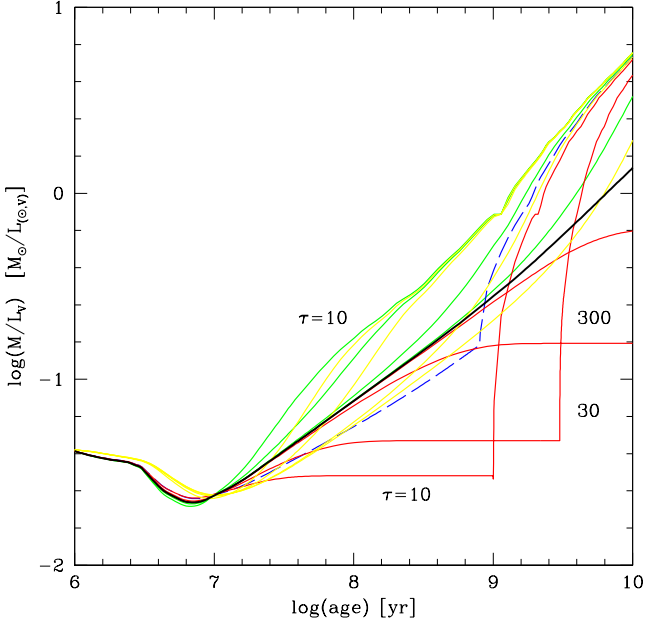


Fig. 3. Predicted mass-to-light ratio in the V-band, M_\star/L_V , for the same models as shown in Fig. 2. Same color codes as in Fig. 1.

use the ratio of the IR to UV luminosity, $L_{\text{IR}}/L_{\text{UV}}$, a quantity known to correlate strongly with the amount of dust attenuation (cf. Meurer et al. 1999).

2.3.3. Predicted IR, sub-mm, and mm fluxes

Given the IR luminosity L_{IR} predicted consistently from the amount of attenuation by dust, it is straightforward to predict the flux at various IR wavelengths, provided a corresponding spectral template for dust emission is adopted. We simply assumed standard modified black-body spectra described by $F_\nu \propto \nu^\beta B_\nu(T_d)$, with a fixed value of $\beta = 2$ and three different dust temperatures $T_d = (25, 35, 45)$ K, which span the range of observed dust temperatures in nearby and distant galaxies. The modified black-body is scaled to L_{IR} computed from 8 to 1000 μm (rest frame). From this, we determine the predicted IR fluxes in bands corresponding to observations with Herschel (PACS and SPIRE bands), several sub-mm bands (350, 450, 850, 870 μm), 1.2 and 2 mm bands, and ALMA bands 1-10 (corresponding to ~ 8.1 to 0.35 mm).

3. Dependence of the physical parameters on the assumed star formation histories

To illustrate and discuss the dependence of the physical parameters on the assumed star formation histories we here choose the largest sample comprising 705 B-drop galaxies. The general behavior discussed here is also found for most of the other samples at $z \sim 3, 5$, and 6. Some results for other redshifts are discussed in Sect. 5.

3.1. Comparison of physical parameters

It is well known that the physical parameters determined from broad-band SED fits depend on assumptions such as the star for-

mation history. In dBSS12 we have shown how quantities such as the stellar mass, age, dust reddening, and SFR depend on this assumption and how they are modified with the inclusion of nebular emission. Here we briefly illustrate the dependence of the main physical parameters on SFH, including in particular the new histories explored in this paper (exponentially rising and delayed SFH; cf. Table 1).

Figures 4 to 7 show how the M_\star , age, A_V , and SFR derived for different assumptions on SFH compare to models assuming exponentially declining star formation histories (our model A) for our largest sample, the 705 B-drop galaxies. This model is taken as a reference, since it generally provides the best fits for the vast majority of galaxies analyzed here (cf. below). For all models except for SFR=const (model B), we include the effects of nebular emission. Model B, called REF in dBSS12, serves as a “reference” model to ease comparisons with other studies in the literature assuming constant star formation, and neglecting nebular emission. When nebular emission is added to model B, this does not lead to very different parameters (cf. dBSS12).

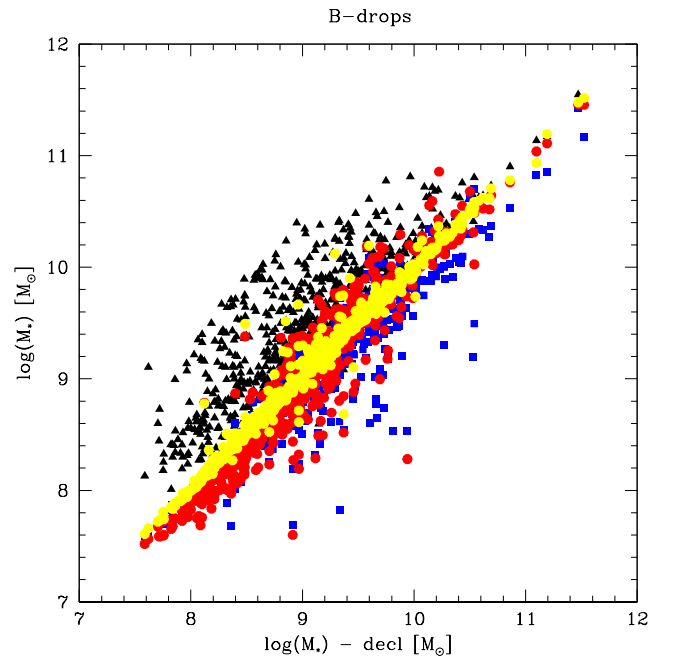


Fig. 4. Comparison of the median stellar masses of our $z \sim 4$ sample with 705 galaxies derived from SED fits assuming the star formation histories listed in Table 1. The masses are compared to those derived from model A, plotted on the x-axis. Black triangles show model B with constant SFR, blue and red symbols the rising histories (model C and D respectively), yellow circles show the delayed SFHs (model E). For each model the same number of galaxies are plotted. Invisible data points are hidden close to the one-to-one relation.

Figure 4 shows that most models yield similar stellar masses, as already known from earlier studies (Yabe et al. 2009). The largest differences are found with respect to models assuming constant star formation and a minimum age of 50 Myr (model B), which yield generally higher stellar masses. On average we find masses lower by a factor ~ 3 at $z \sim 4$ for declining SFHs (model A), where half of this effect is due to inclusion of nebular emission (cf. de Barros et al. 2012). The difference is mostly due to the average shift towards younger ages, which have a lower mass-to-light ratio, as shown in Fig. 3. It is immediately appar-

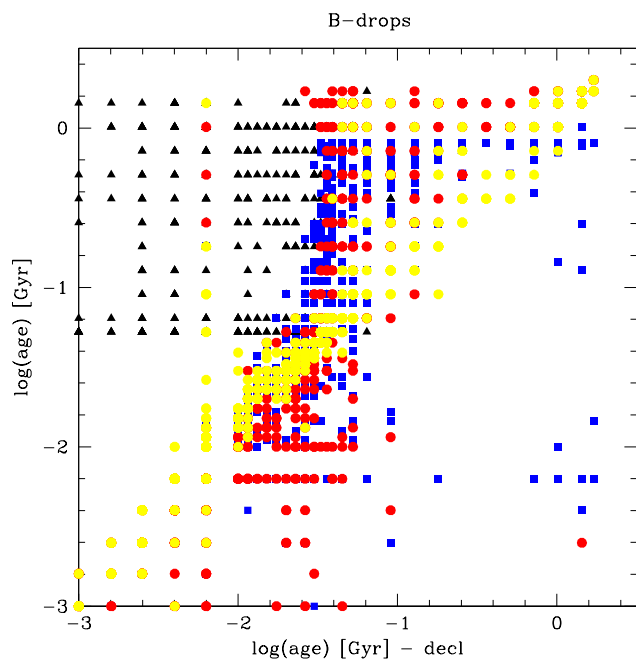


Fig. 5. Same as Fig. 4 for the stellar age, defined since the onset of star formation. For each model the same number of galaxies are plotted. Invisible data points may be hidden, especially under the yellow symbols of model E plotted last, due to discrete age values.

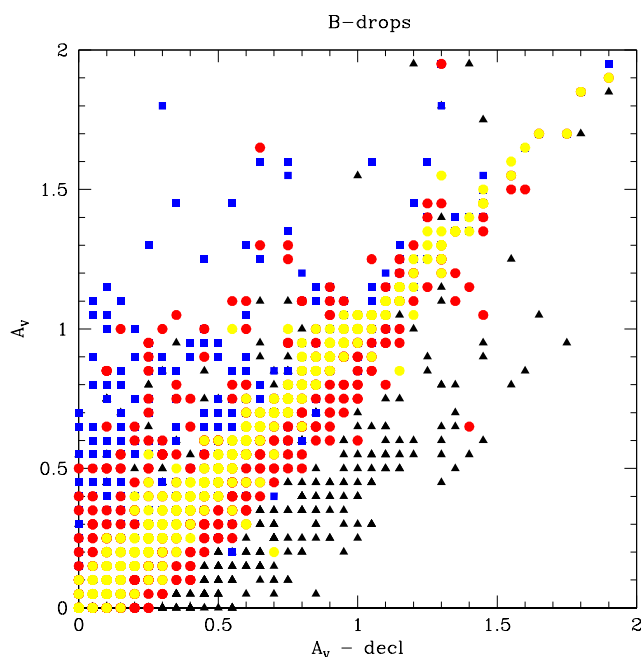


Fig. 6. Same as Fig. 4 for the attenuation A_V . For each model the same number of galaxies are plotted. Invisible data points may be hidden, especially under the yellow symbols of model E plotted last, due to discrete age values.

ent that the models with delayed star formation histories (model E) yields very similar results to model A. Exponentially rising SFHs with variable timescales (model D) and the rapidly rising history from Finlator et al. (2011) (model C) give also comparable stellar masses, although with a larger scatter, when compared

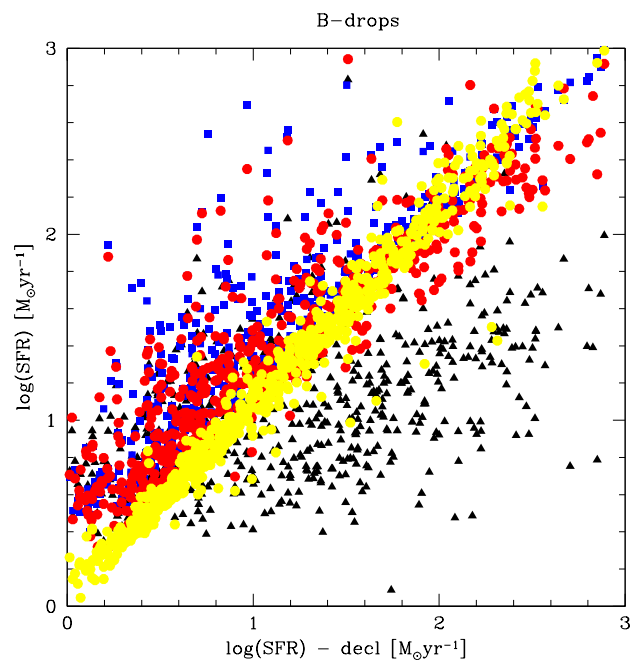


Fig. 7. Same as Fig. 4 for the current star formation rate SFR.

to model A. In short, all the models with variable SFHs and nebular emission considered here yield quite similar stellar masses, which are on average lower than those obtained from standard models without nebular emission.

Age is notoriously known to be sensitive to models assumptions (e.g. Papovich et al. 2001; Yabe et al. 2009). Indeed, absolute ages predicted by different models can differ by orders of magnitude, as shown in Fig. 5. Overall models with delayed SF (E) show again quite similar results to those with exponentially decreasing histories (A). The behavior of the rising SFHs (C and D) is quite comparable. By construction, model B yields only stellar ages ≥ 50 Myr. Whereas for exponentially declining and delayed SFHs most objects are best fit with relatively short and comparable timescales τ , the opposite is true for fits with exponentially rising histories. In this case the probability distribution function for τ clearly peaks at the maximum value allowed here ($\tau = 3$ Gyr), which means that a relatively slow growth is preferred for most galaxies. This seems quite natural given the finding that the rising SFH from Finlator et al. (2011) fits on average less well than declining models.

The attenuation predicted by the various models is shown in Fig. 6. As already discussed by dBSS12, constant SF models show generally lower dust attenuation than the exponentially declining models, whereas the rising SFH of Finlator et al. (2011) predicts a higher attenuation on average. Rising star formation histories with variable timescales globally scatter around those assuming declining SF. Again, delayed SFHs give results very similar to those with declining SFHs.

The predicted median SFR of all galaxies are compared in Fig. 7. As expected due to lower dust attenuation and older ages, the models with constant SFR show generally the lowest (current) star formation rates (cf. dBSS12). As before, models A and E are very similar. Finally, assuming rising star formation histories generally implies a higher SFR, due to, first, the lower L_{UV} output per unit SFR (cf. Fig. 2), and, second, to a higher average dust attenuation, needed to redden the UV slope, which is always dominated by the youngest stars.

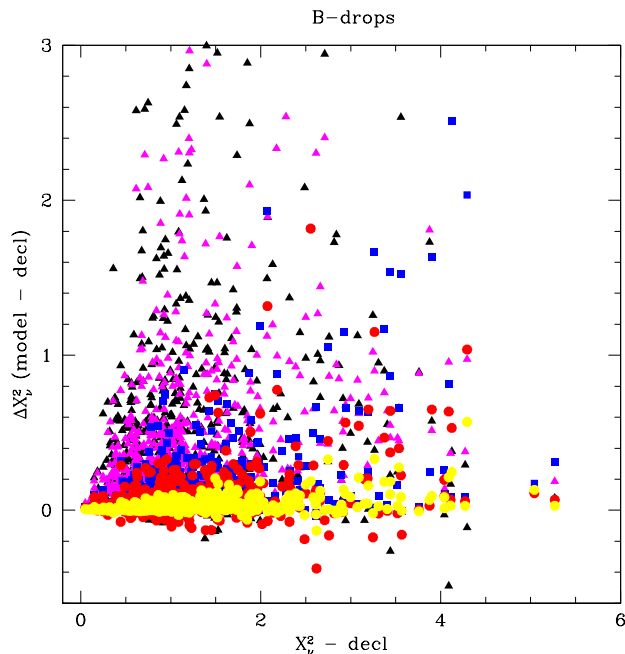


Fig. 8. Comparison of the median value of the reduced χ^2_v for each galaxy of the B-drop sample ($z \sim 4$) computed for different star formation histories and plotted as a function of χ^2_v obtained from model A (declining star formation histories). Same symbols and colors as in previous figures and listed in Table 1.

3.2. Comparison of the fit quality

Figure 8 shows the fit quality of the models expressed by the reduced χ^2_v value² for the $z \sim 4$ sample. Overall, declining star formation histories (model A) give the best fit to most galaxies, and delayed SFHs very similar fits. Exponentially rising histories provide better fits for some objects, but a higher χ^2 on average. Models B and C with constant SFR and rapidly rising star formation yield fits of lower quality for most galaxies.

We have also examined the influence of another reddening law (cf. Sect. 7). Applying the SMC law of Prevot et al. (1984); Bouchet et al. (1985) we find that the majority of galaxies fit less well than with the Calzetti law, both the declining and rising star formation histories (model A, C, and D), although the differences are generally relatively small (cf. Sect. 7).

3.3. Implications for the SFR–mass relation and influence of the minimum age

Figure 9 shows the SFR–mass relation for the 705 B-drop galaxies as derived from the SED fits assuming the five different star formation histories. As already discussed in dBSS12, the models show overall a large scatter and a median specific SFR (SFR/M_\star) above the mean relation derived by Daddi et al. (2007) at $z \sim 2$, also shown for comparison. In part the scatter in this diagram is determined by the possible range of SFR/M_\star predicted for stellar populations with different SFHs and different ages. Indeed, for a given L_{bol}/L_V , probed observationally by L_{UV}/L_V , the ratio SFR/M_\star varies by ~ 2 orders of magnitude between young ages and $t \lesssim 1$ Gyr for constant SFR models, and more for declining

or delayed star formation histories (Figs. 2 and 3). Of course, since reddening also modifies L_{UV}/L_V , this adds further scatter.

As expected, the delayed SFH yields basically identical results to the declining histories. Rising histories (model D) occupy a similar domain as the other variable SFHs (models A, C, E), except for the *absence of galaxies below* the mean relation from Daddi et al. (2007). This is simply due to the fact that star formation cannot decrease in this model and for model B (constant SFR). Hence situations where the current SFR is low, but the UV flux is still present from somewhat older stars (e.g. B-type stars with lifetimes up to ~ 100 Myr) are not possible for these SFHs (cf. Fig. 2). Objects well below the SFR–mass relation require obviously decreasing star formation histories, or some shut-off of star formation.

The *upper boundary* of the SFR– M_\star plot, parallel to the indicated $z \sim 2$ relation, is determined by the minimum age, and by dust attenuation. Indeed, young ages imply lower masses and a higher SFR from simple considerations of SFR/UV and mass/light ratios (cf. Figs. 2 and 3, also McLure et al. 2011).

Since age is kept free in all our models³ except for model B where we assume a minimum age of 50 Myr, and since some the median ages obtained are relatively young (e.g. compared to typical dynamical timescales of disks; cf. dBSS12) it is interesting to explore how the main physical parameters and the SFR– M_\star relation change when introducing a prior on the minimum age (or equivalently on the formation redshift) for all models.

The effect of fixing the minimum age to $t_{\text{min}} = 50$ Myr in the SED fits with exponentially declining and rising star formation histories (models A and D) on the SFR–mass relation is shown in Fig. 10. In short, for the declining SFHs the *upper boundary* becomes now identical to the one obtained with $\text{SFR}=\text{const}$ (model B), as expected, since declining SFHs include long timescales τ for which the star formation history becomes undistinguishable from constant, and since $t_{\text{min}} = 50$ Myr sets the maximum SFR/UV output. In contrast, for rising SFHs the upper boundary is found to be higher by a factor ~ 3 approximately. Again, this simply due to the less efficient UV output per unit SFR (or higher SFR/UV ratio) of the youngest stars, which always dominate the SFR for such star formation histories (Fig. 2). The *lower boundary* of the SFR–mass relation remains of course unchanged by changes of the minimum age. In conclusion, introducing a minimum age affects in different ways the SFR– M_\star relation, depending on the SFH.

On average, i.e. for the entire sample of 705 B-drop galaxies, the median age and mass increase by a factor ~ 2 , whereas SFR and A_V decrease by a factor ~ 2 , when the prior $t_{\text{min}} = 50$ Myr is introduced. For the rising histories (model D) the median age increases by a factor ~ 5 , SFR decreases by 1.5, stellar mass increases by a factor 2. On the other hand the dust attenuation, both of individual galaxies and on average, remain very similar, with interesting implications on the predicted IR luminosity (see Sect. 4.4).

To conclude this section we note that SED fits using models with variable star formation histories imply a fairly large scatter in the SFR–mass relation for LBGs at $z \geq 3$, as shown here and in dBSS12. However, it must be pointed out that the amount of scatter cannot directly be translated into observable quantities such as UV and/or IR luminosity, which are commonly used as SFR indicators. Indeed, as we will show below (Sect. 4.3), a much smaller scatter is expected in terms of observed UV+IR luminosity.

² Here χ^2_v is defined as $\chi^2/(N_{\text{filt}} - 1)$, where N_{filt} is the number of filters for which data is available for the galaxy, including non-detections.

³ The only age limitation is given by the age of the Universe.

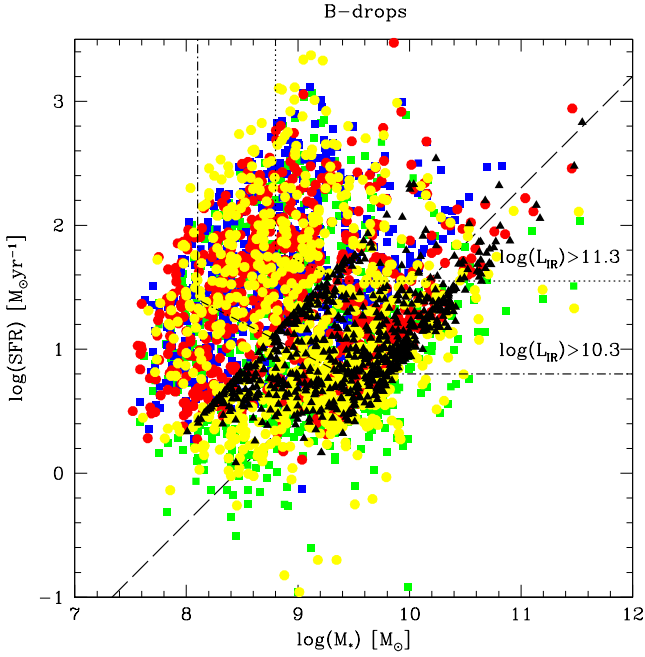


Fig. 9. Current SFR as a function of stellar mass of the $z \sim 4$ LBGs obtained for different SF histories. Same symbols as Fig. 4. The dotted and dash-dotted lines delimit the area above which galaxies with $L_{\text{IR}} \gtrsim 2 \times 10^{11} L_{\odot}$ (or equivalently a flux > 0.2 mJy in ALMA band 7 **which wavelength** for $T_d = 35$ K) or $> 2 \times 10^{10} L_{\odot}$, respectively, are found. The dashed line shows the SFR–mass relation at $z \sim 2$ for comparison.

4. Predicted IR-mm emission

4.1. IR luminosity and constraints on UV attenuation by dust

Figure 11 shows the infrared luminosity predicted by the different models for the $z \sim 4$ sample, Fig. 12 the corresponding histogram of $L_{\text{IR}}/L_{\text{UV}}$ ⁴. Since some galaxies have a median $A_V = 0$ and hence no UV light is absorbed, their predicted median IR luminosity is $L_{\text{IR}} = 0$. Such galaxies are not shown on these plots; their percentage ranges from 24% for model B (with constant SFR) to 10% for model C, which has the highest median L_{IR} . Due to the adopted discretisation in A_V , the lowest, non-zero extinction $A_V = 0.05$ corresponds to $\log(L_{\text{IR}}/L_{\text{UV}}) \approx -0.85$, as seen e.g. in Fig. 26.

As could be expected from the behavior of the UV attenuation, the models with constant SFR predict generally significantly lower L_{IR} than models with different star formation histories. On average, the highest L_{IR} is predicted for steeply rising SF of Finlator et al. (2011), followed by the exponentially rising model D, and model A and E with very similar average IR luminosities. Clearly, if L_{IR} can be determined with sufficient accuracy from observations, it should be possible to distinguish different models for individual galaxies, as well as statistically for large enough samples.

Most importantly the IR/UV ratio allows one to measure the UV attenuation as well known (cf. Buat et al. 2005; Iglesias-Páramo et al. 2007, and references therein), and this independently of the assumed SF history and of the extinction law. To demonstrate this we compute the UV attenuation factor f_{UV} defined by the ratio of the intrinsic (emitted) over the observed

⁴ Here L_{UV} is essentially model independent (except for the photometric redshift), since determined by the observed UV magnitude.

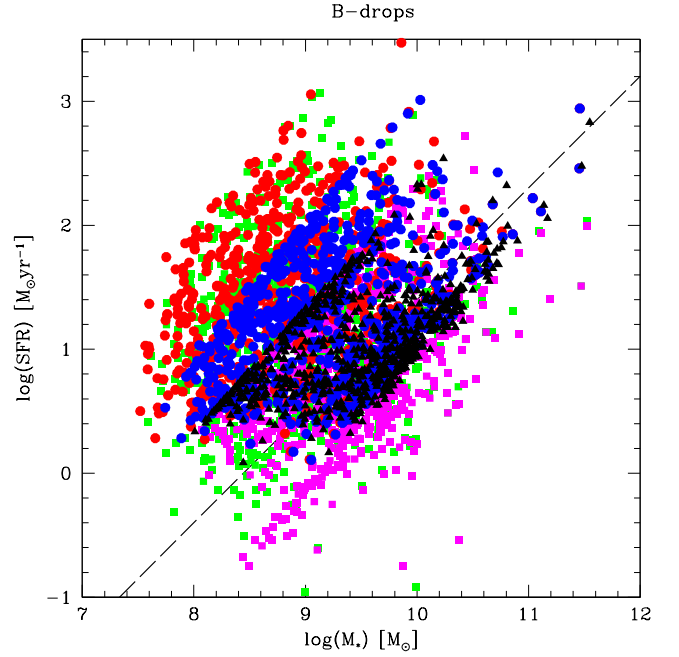


Fig. 10. Effect of adopting a minimum age prior on the SFR–mass relation. Green (red) show the models with declining (rising) SFHs, as in Fig. 9. Including the prior $t > 50$ Myr yields the magenta (dark blue) points for the declining (rising) SFHs. Note the decrease of the upper boundary of the SFR– M_* relation, but less so for rising SFH than for declining ones. Black triangles stand for model B with SFR=const. The dashed line shows the SFR–mass relation at $z \sim 2$ for comparison.

UV luminosity, i.e.

$$f_{\text{UV}} = L_{\text{UV}}^{\text{int}}/L_{\text{UV}}. \quad (1)$$

This quantity is shown in Fig. 13 for all galaxies of the $z \sim 4$ sample, for all star formation histories and for the Calzetti attenuation and SMC extinction curve. The figure clearly shows a tight correlation between f_{UV} and $L_{\text{IR}}/L_{\text{UV}}$ independently of the assumed star formation history and of the extinction/attenuation law, a behavior well known from the work of Buat et al. (2005); Iglesias-Páramo et al. (2007); Boquien et al. (2012) and others. The UV attenuation factor (defined here at 1800 \AA) can simply be described by

$$\log(f_{\text{UV}}) = 0.24 + 0.44x + 0.16x^2 \quad (2)$$

where $x = \log(L_{\text{IR}}/L_{\text{UV}})$. For a specific attenuation law this can of course be translated into quantities such as A_V . For example, for the Calzetti law one has $A_V = 2.5(R_V/k_\lambda) \log f_{\text{UV}} = 1.08 \log f_{\text{UV}}$. Such a simple relation is quite naturally obtained, since the bulk of the energy reemitted in the IR after absorption by dust is also produced by the same stars contributing the bulk of the UV emission. More complicated relations could be expected when e.g. older stellar populations such as AGB or RGB stars contribute to dust emission, as appears to be the case in low redshift galaxies (Buat et al. 2005).

In short, measurements of $L_{\text{IR}}/L_{\text{UV}}$ of individual LBGs provide a direct measure of their UV attenuation, which should allow us to distinguish certain star formation histories, and in particular to test the systematic shift in physical properties predicted between models assuming long star formation timescales (constant SFR) and variable (rising or declining) star formation

histories. However, additional observational constraints, such as emission line strengths discussed later, may be necessary to distinguish between among variable SFHs, since both rising and declining histories yield fairly similar predictions for many physical parameters (cf. dBSS12 and above).

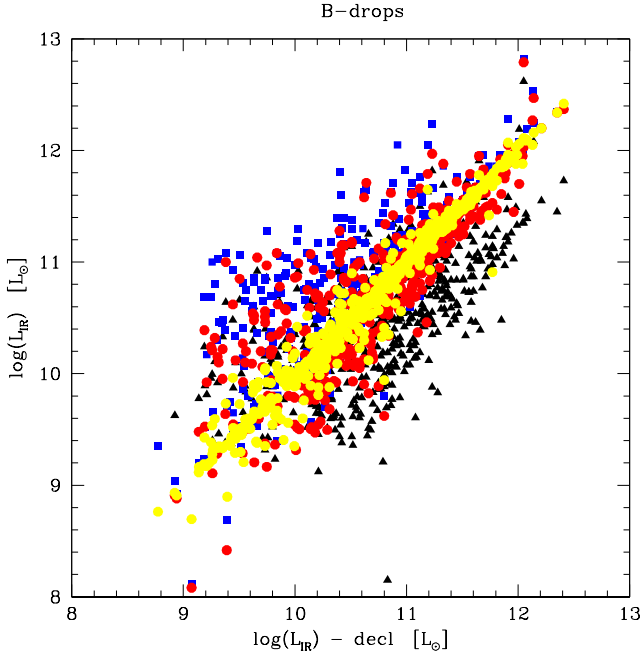


Fig. 11. Same as Fig. 4 for the predicted IR luminosity.

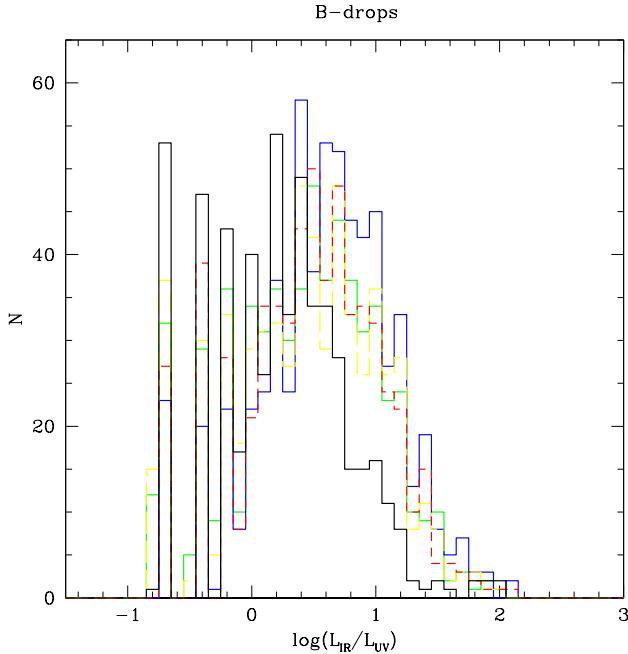


Fig. 12. Histogram of the predicted median IR/UV luminosity ratio for the $z \sim 4$ sample from models assuming different star formation histories (Model A: green dashed line; model B: solid black; model C: solid blue; model D: red dashed; model E: yellow dashed).

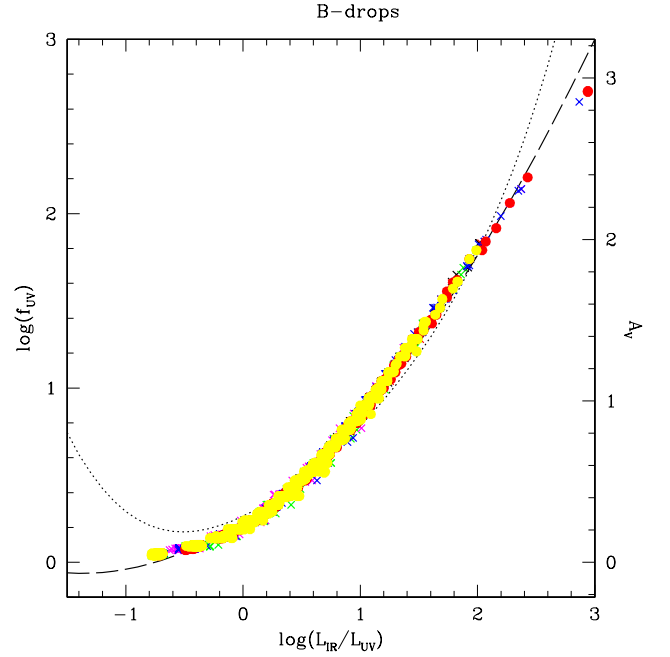


Fig. 13. UV attenuation factor f_{UV} as a function of the predicted ratio of the IR/UV luminosity. A tight relation, fitted by Eq. 1 and shown by the dashed line, is obtained independently of the assumed SF history and of the extinction law. For comparison the relation determined by Boquien et al. (2012) is shown by the dotted line. The corresponding attenuation A_V assuming the Calzetti law is shown on the right scale.

4.2. IR and UV luminosity as tracers of the SFR in light of different star formation histories

Often the IR luminosity or the sum of IR+UV luminosity are used as a measure of the star formation rate (e.g. Kennicutt 1998; Burgarella et al. 2005; Reddy et al. 2010, 2012). The basic assumptions made for such conversions are that of constant SFR and an age of $\gtrsim 50$ –100 Myr, necessary to reach an equilibrium output for the UV and bolometric luminosities (see also Fig. 2). The determination of the SFR from L_{IR} also assumes that the total (stellar) bolometric luminosity is reemitted in the infrared domain, which requires significant dust attenuation. Obviously the above assumptions cannot be valid in general, and in particular they are not compatible with the different star formation histories explored in this paper.

In Figs. 14 and 15 we show the predicted IR and IR+UV luminosity respectively as a function of the (current) SFR determined from fitting our models to the sample of $z \sim 4$ galaxies. The “standard” SFR(IR) calibration given by Kennicutt (1998) – based on the bolometric luminosity – is also indicated for comparison. Overall quite large deviations from the simple calibration are obtained for L_{IR} –SFR, and smaller deviations for $(L_{IR} + L_{UV})$ –SFR. As expected model fits assuming constant SF (model B) agree very well with the Kennicutt relation when the IR+UV luminosity, providing a very good measure of the bolometric luminosity, is used. However, for galaxies with $SFR \lesssim 20$ –30 $M_{\odot} \text{ yr}^{-1}$, the predicted IR luminosity is decreased with the respect to this relation. This is simply due to the fact that these galaxies are not found to be dusty enough to reprocess a significant fraction of their UV light into IR radiation. This is also clearly illustrated by the large uncertainties in L_{IR} , which can reach values down to 0 if the pdf of A_V does so. This ef-

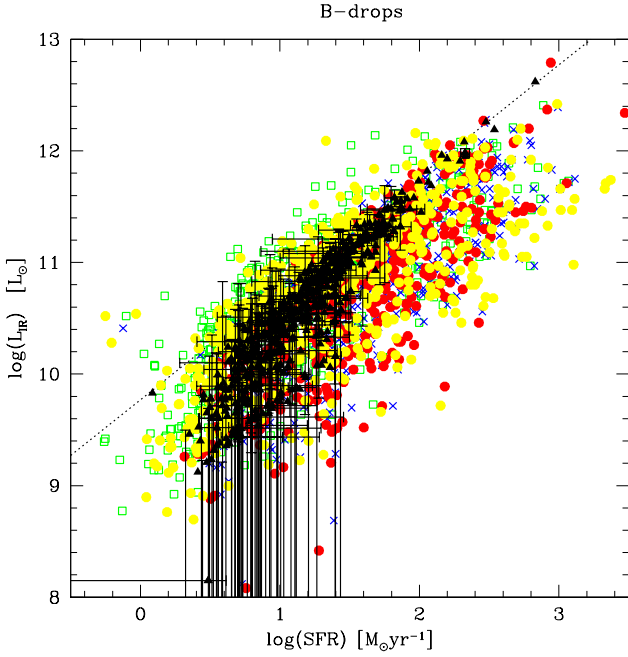


Fig. 14. Median IR luminosity L_{IR} predicted for the B-drop sample as a function of the median SFR obtained from the SED fits for the models with different star formation histories. Results from exponentially declining models (A) are plotted with green squares. The remaining symbols and colors are the same as in previous figures. For the constant SFR model the results, shown as black triangles, we also plot the 68% confidence range; for clarity these error bars are shown only for 1/6 randomly chosen galaxies of the sample. The dotted line indicates the SFR(IR) calibration of Kennicutt (1998).

fect, shown here for $\text{SFR}=\text{const}$, is present for all star formation histories.

More generally, for varying star formation histories, both the IR and the IR+UV luminosity predicted by model fits are *lower* than expected from the Kennicutt relation between SFR and luminosity (Figs. 14 and 15). Two effects explain these differences. First, dust extinction needs to be high enough for L_{IR} to be a good tracer of the total SFR (cf. above). Second, the ages are younger than the time needed to reach the bolometric output assumed by Kennicutt (1998). Typically, this is the case for ages $t/\tau \lesssim 1$ for declining SFHs, somewhat longer for delayed and rising star formation histories, and ~ 100 Myr for constant SF, as illustrated in Fig. 2. The second effect explains the values of $L_{\text{IR}} + L_{\text{UV}}$ below the canonical L_{IR} –SFR relation. Added to that, the first effect further diminishes L_{IR} for galaxies with lower SFR, as already explained above. In some cases, although for a small fraction of galaxies, we find that the predicted IR or IR+UV luminosity is *higher* than what is expected from the Kennicutt (1998) relation using the model SFR. This is found with declining or delayed star formation histories for galaxies where $t/\tau \gg 1$, i.e. where star formation starts to decrease but longer-lived stars still contribute to the bolometric luminosity. These objects are expected to show weak emission lines, i.e. they should include galaxies from the category of “quiescent” LBGs identified by dBSS12, and which can also be recognized by their 3.6 micron excess, if at $z \sim 3.8$ –5.

Of course it should be noted that the SFR shown in these plots is not a direct observable, since it corresponds to the current SFR determined from the broad-band SED fits, and since

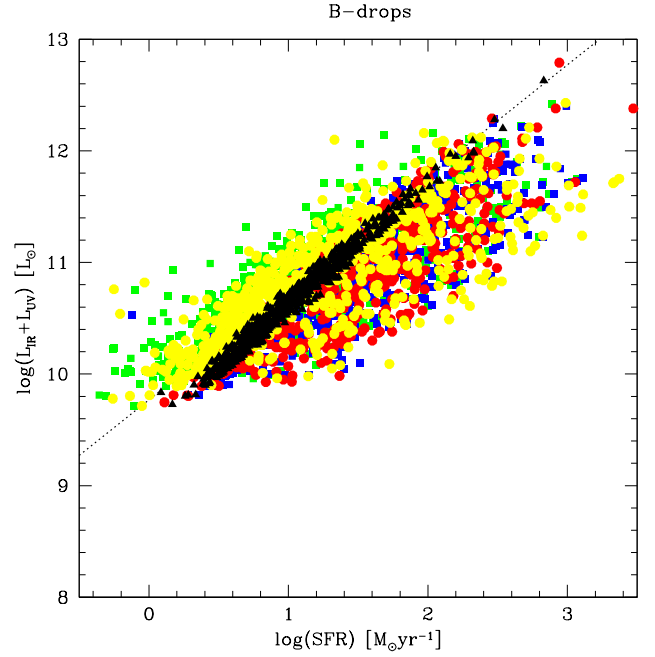


Fig. 15. Same as Fig. 14 for the IR+UV luminosity, which provides a better approximation of the bolometric luminosity.

the SFR derived in this manner depends itself on model assumptions, such as the assumed star formation history (cf. Sect. 3 and Fig. 7). Observationally the best measure of the current SFR obtained from the SED fits should be the one measured by hydrogen recombination lines (e.g. $\text{SFR}(\text{H}\alpha)$), once corrected for dust attenuation, since these emission lines trace best short-lived massive stars. From the $\text{H}\alpha$ flux predicted by our SED models, the consistency with $\text{SFR}(\text{H}\alpha)$ can indeed be verified.

The main conclusions to be drawn from Figs. 14 and 15 is that IR or (IR+UV) SFR calibrations assuming constant star formation over long timescales should be used with caution for the interpretation of high- z star forming galaxies (e.g. LBGs), since they are susceptible to variations of the star formation history on short timescales, for which there are good indications (see dBSS12 and this paper). In any case, the effects discussed here need to be taken into account to properly predict the IR emission of LBGs and for comparisons with observations. Possible problems related to the use of inconsistent SFR indicators, and implications on the SFR–mass relation are discussed below (Sects. 4.3 and 7.2).

4.3. Implications on the SFR–mass relation

Fig. 16 shows the SFR–mass relation with SFR transformed to direct observables, namely the sum of the UV and IR luminosity. Compared to the SFR– M_\star relation plotted in Fig. 9, which shows a very large scatter (with an upper bound up to 2 dex above the mean relation at $z \sim 2$) for models allowing for young ages and for variable star formation histories, the scatter in this relation is now significantly reduced, approximately by one order of magnitude, as judged by the upper boundary. The reason is again due to the fact that the models with the highest current SFR/ M_\star values correspond to relatively young ages, where the bolometric output per SFR is lower (Fig. 2). Hence the smaller dynamic range in bolometric luminosity, which is well approximated by $L_{\text{IR}} + L_{\text{UV}}$. In other words, although the intrinsic, cur-

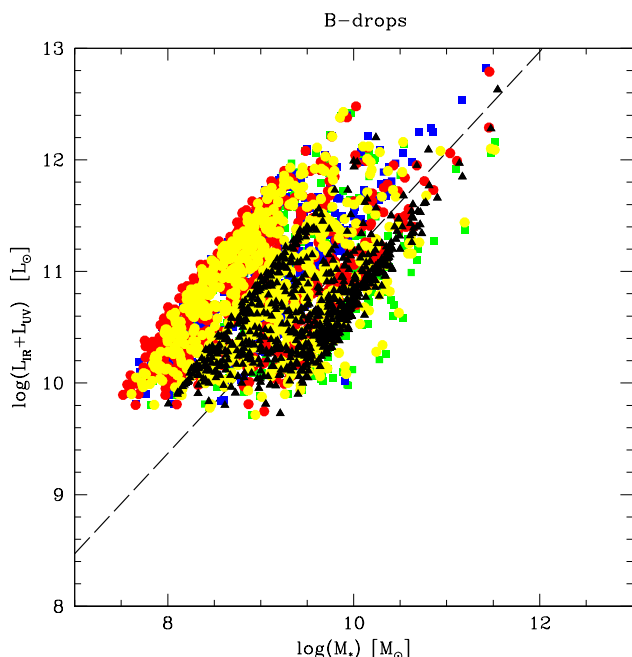


Fig. 16. Median UV+IR luminosity predicted consistently for the B-drop sample as a function of the median stellar mass obtained from the SED fits for the models with different star formation histories. Note that the predicted scatter in luminosity is much smaller than the one in the true, underlying SFR shown in Fig. 9, since the corresponding IR luminosity is computed consistently with the assumed SF timescales and ages. The dashed line indicates the expected UV+IR luminosity expected assuming the SFR–mass relation at $z \sim 2$ from Daddi et al. (2007) and the SFR(IR) calibration of Kennicutt (1998).

rent SFR may show a wide dispersion, the SFR one would infer from the UV+IR luminosity assuming “standard” SFR conversion factors would show a much smaller dispersion! This demonstrates that the finding of a small dispersion in the bolometric luminosity– M_* plane does not exclude a high dispersion between current SFR and stellar mass, and objects with very high values of the specific star formation rate, SFR/M_* .

4.4. Influence of the minimum age on the dust attenuation and IR luminosity

How does the choice of a minimum age affect the derived attenuation and hence the predicted IR luminosity? Figure 17 shows the result of this exercise for the exponentially declining and rising SFHs (model A and D). We find that introducing a lower limit t_{\min} (age prior) leaves the predicted IR luminosity of LBGs unchanged on average for the rising star formation histories, whereas L_{IR} diminishes for declining SFHs. The basic reason for this behavior is the following: since for rising SFHs the intrinsic UV emission does not decrease when the age is increased, the attenuation and hence their IR luminosity remains comparable for most galaxies. In contrast, for decreasing star formation histories an older age allows one to reproduce the SED with a lower attenuation (cf. the well known age–extinction degeneracy). Thus a lower L_{IR} , comparable to the values predicted for the constant SF model with the same minimum age, is expected for this case. In other words, although the predicted L_{IR} depends in general on assumptions on the minimum age of stellar populations, this is not the case for rising star formation histories, which con-

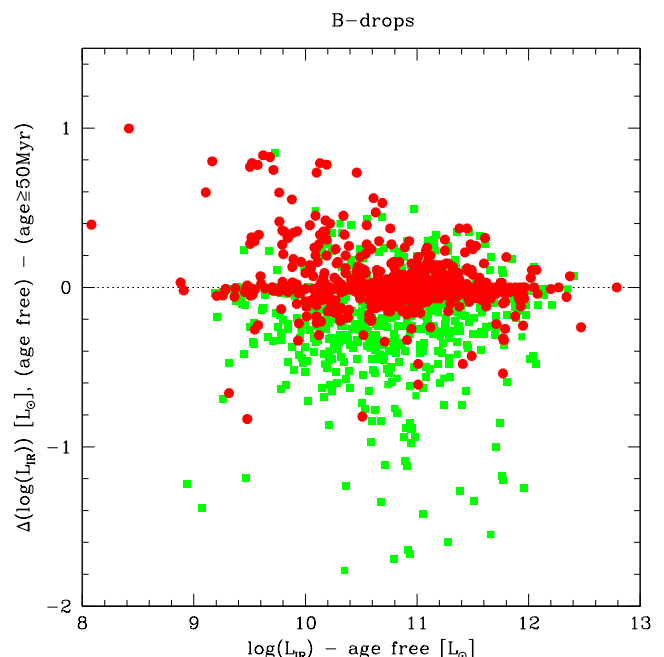


Fig. 17. Effect of adopting an age prior (minimum age $t > 50$ Myr) on the predicted IR luminosity for declining (green, model A) and rising (red, model D) histories. We plot the difference in $\log(L_{\text{IR}})$ between the unconstrained model and the one with age prior as a function of the latter. On average declining SFH show lower L_{IR} whereas rising histories predict basically the same, or even higher IR luminosities. Rising SFHs case can thus be distinguished from constant SFR, even if age priors apply.

tently predict a higher UV attenuation and hence IR luminosities than constant SF or declining histories. A similar distinction was already seen in the SFR–mass relation (Fig. 10). Measuring L_{IR} can help test/constrain these different scenarios.

5. Predictions for ALMA

5.1. Continuum flux predictions

In Fig. 18 we show predicted fluxes for the B-drop samples in one of the ALMA bands (band 7 covering $\sim 0.8\text{--}1.1\text{mm}$) available during the early ALMA cycles. As explained in Sect. 2 these fluxes are derived from the predicted IR emission, L_{IR} discussed above, with the assumption of modified black bodies with a typical dust temperature of $T_d = 35\text{ K}$ and $\beta = 2$. Changes of the dust temperature by $\pm 10\text{ K}$ correspond to a change of the flux by a factor $\sim 2.5\text{--}2.8$ approximately. At this redshift ($z \sim 4$) the emission increases (decreases) with decreasing (increasing) dust temperature in this band, since the peak of the spectrum lies at shorter wavelengths than band 7 considered here.

Fig. 18 clearly shows the significant flux differences predicted by models assuming different star formation histories. If the dust properties (temperature and exponent β) do not change, the IR-mm fluxes simply reflect the differences in IR luminosity predicted by the models, as already discussed in Sect. 4. While the majority of the $z \sim 4$ LBGs show fluxes below the sensitivity limit reached with short (60 s) exposures with the full ALMA array, approximately half of the sample should be detectable with 30min exposures. In any case, already with the current, incomplete ALMA array the brighter part of the distribution should be detectable. Such measurements will provide badly needed, di-

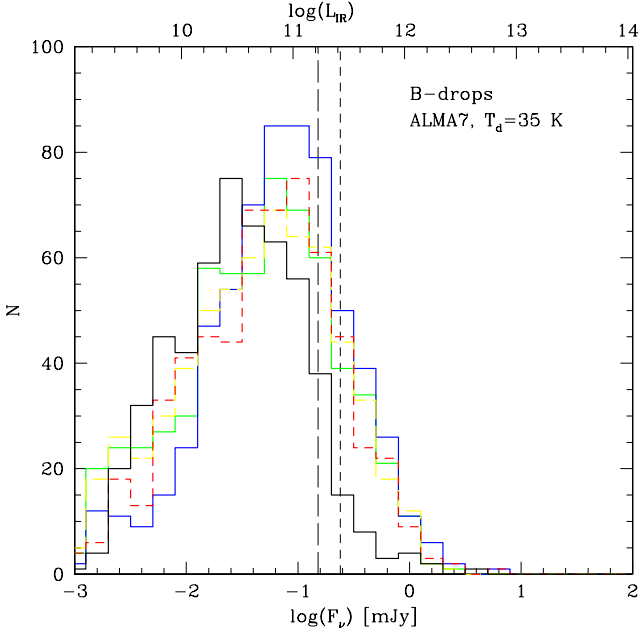


Fig. 18. Predicted histogram of median dust continuum fluxes in the ALMA band 7 (0.8–1.1 mm) for the B-drop sample from models assuming different star formation histories. The predictions are plotted for modified black bodies with $T_d = 35$ K and $\beta = 2..$ Same color coding as in Fig. 21. The vertical lines indicate the continuum sensitivity for an integration time of 60 s with the full array (long dashed), and with 32 antennae available for the ALMA cycle 1 (short dashed). The upper axis indicates the corresponding IR luminosity. Changes of the dust temperature by ± 10 K correspond to a change of the flux by a factor ~ 2.5 – 2.8 approximately.

rect measurements of the UV attenuation of $z \sim 4$ LBGs and very useful tests/constraints on the SED models and on the star formation histories of these distant galaxies.

When selecting galaxies by their IR luminosity, which part of the SFR–mass diagram such as Fig. 9 do we probe? Naively one would expect this to translate to a simple limit in SFR. However, since SFR/L_{IR} is a priori not constant, i.e. age dependent, and since L_{IR} also depends on the amount of dust attenuation, the limit is more complicated. This domain is e.g. illustrated for $L_{\text{IR}} > 2 \times 10^{11} L_{\odot}$ by the dashed line in Fig. 9. Whereas this criterium selects all massive galaxies with $\text{SFR} \gtrsim 35 M_{\odot} \text{ yr}^{-1}$, such galaxies with $M \lesssim 6 \times 10^8 M_{\odot}$ have relatively young populations and less dust, which implies a lower IR luminosity for the same SFR, below the IR luminosity limit. Although the detailed shape of curves of $L_{\text{IR}} = \text{const}$ in Fig. 9 depend somewhat on the value of L_{IR} , their qualitative behaviour is similar.

5.2. Evolution of the IR luminosity with redshift

The typical predicted IR luminosities at $z \sim 4$ are shown in Fig. 19 as a function of the absolute UV magnitude (here M_{1500} for comparison with dBSS12) for model A, i.e. declining star formation histories. The figure shows the 2D probability distribution function (pdf), the median values for each galaxy (white circles), and the median of the pdf in bins of UV magnitude (red stars). As mentioned earlier, the pdf also includes a tail to very low IR luminosities, set somewhat arbitrarily to L_{IR} values outside the

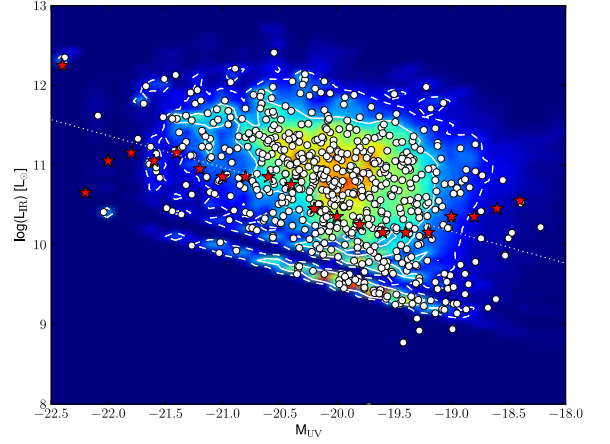


Fig. 19. Predicted IR luminosity as a function of the absolute UV magnitude for the B-drop sample ($z \sim 4$) assuming declining star formation histories (model A). Colors show the full 2D probability distribution function (pdf) of the sample. The solid (dashed) lines encircle the 60 (90) % confidence range. The median values of each galaxy with a median $A_V \geq 0.05$ are shown as white circles. The median of the pdf in bins of UV magnitude is shown as red stars. The dotted line shows, for comparison, the expected L_{IR} when assuming the standard SFR(UV) and SFR(IR) relations of Kennicutt (1998), and $\text{SFR}(\text{UV}) = \text{SFR}(\text{IR})$.

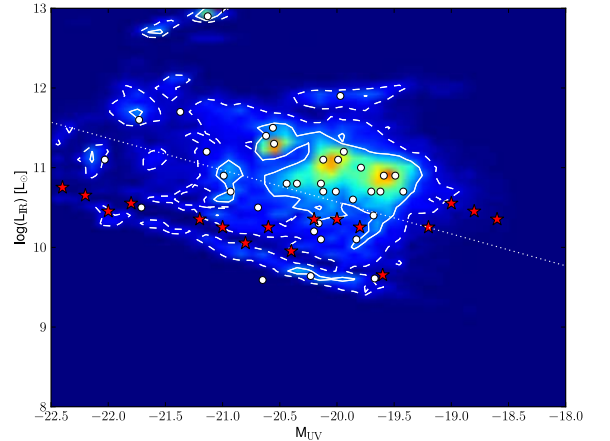


Fig. 20. Same as Fig. 19, for the i-drop sample with 60 galaxies at higher redshift ($z \sim 6$). Note the significant decrease in the median $L_{\text{IR}}-M_{\text{UV}}$ relation compared to $z \sim 4$, due to the decrease of the median dust attenuation found with increasing redshift (cf. dBSS12).

plot, since some of the SED fits also allow for zero extinction. This explains why the median IR luminosity (red stars) is shifted towards lower values than the peak of the pdf. Incidentally, at $z \sim 4$, the median L_{IR} for model A is found to be quite close to the IR luminosity predicted from the UV magnitude using the standard SFR(UV) and SFR(IR) relations of Kennicutt (1998), and assuming $\text{SFR}(\text{UV}) = \text{SFR}(\text{IR})$, as shown by the dotted line. On average we find that the UV brightest galaxies are also expected to be brightest in the IR, in agreement with Reddy et al. (2012); González et al. (2012) and other studies. Typical median

luminosities are of the order of $L_{\text{IR}} \sim 10^{10-11} L_{\odot}$ for model A (cf. Fig. 18).

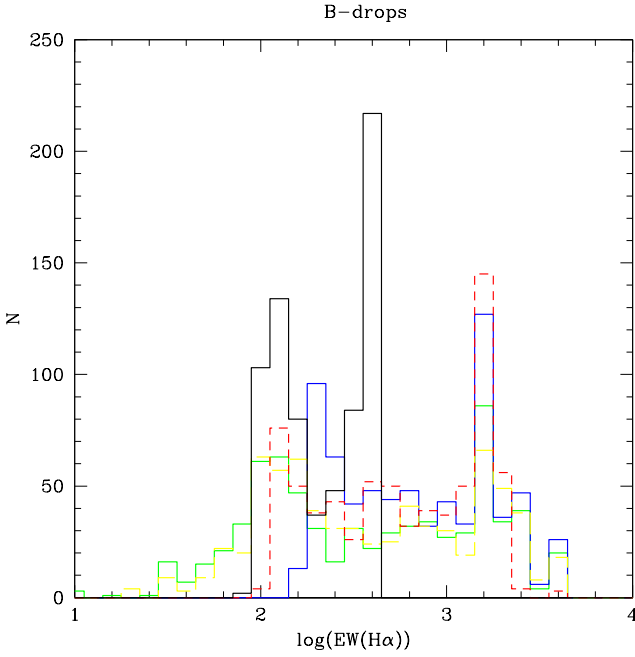


Fig. 21. Histogram of the predicted median (rest-frame) $H\alpha$ equivalent widths for the $z \sim 4$ sample from models assuming different star formation histories (Model A: green solid line; model B: solid black; model C: solid blue; model D: red dashed; model E: yellow dashed).

In Fig. 20 we show the IR luminosity for the i-drop sample ($z \sim 6$) predicted from model A. It should be noted that a higher fraction of the 60 objects of this sample are found with a median attenuation of zero (below our minimum non-zero value of $A_V = 0.05$), implying thus a median L_{IR} outside this plot. In other words the complete pdf has a secondary peak at low values of L_{IR} , not shown here, which explains – as for Fig. 19 – the shift of the median of the sample (red stars) with respect to the apparent peak of the pdf. Clearly, the predicted IR luminosity of $z \sim 6$ LBGs is lower by a factor ~ 3 –4 at most UV magnitudes, due to the lower dust attenuation at high redshift (see dBSS12 for more details). However, despite the lower reddening, the SED fits show that galaxies at $z \geq 6$ with dust exist quite likely, even at these high redshifts (cf. dBSS12, also Schaerer & de Barros 2010). Indeed, these studies show a clear trend of increasing average dust attenuation with galaxy mass, at all redshifts.

6. Predicted (rest-frame) optical emission lines

Since one of the main features of our SED analysis is the treatment of nebular lines, whose effects turns out to be not negligible for approximately two thirds of the LBGs (cf. dBSS12), it is obviously of interest to examine the predicted strength of these emission lines, and to test these predictions observationally. From the 63 lines from the (rest-frame) UV, optical and near-IR domain included in our models, we illustrate here $H\alpha$, among the strongest optical lines, and $[\text{O II}] \lambda 3727$, the bluest optical line. Their predicted equivalent width distribution for the B-drop sample and for the different star formation histories are shown in Figs. 21 and 22.

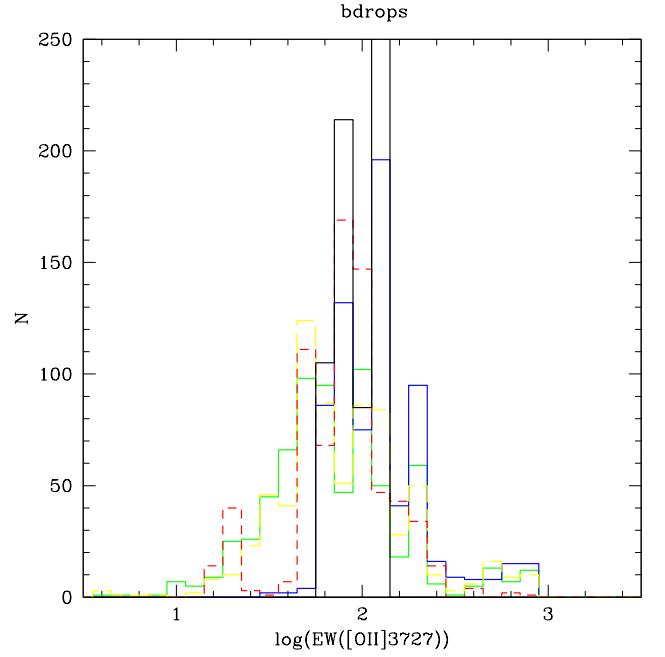


Fig. 22. Same as Fig. 21 for the (rest-frame) $[\text{O II}] \lambda 3727$ equivalent width.

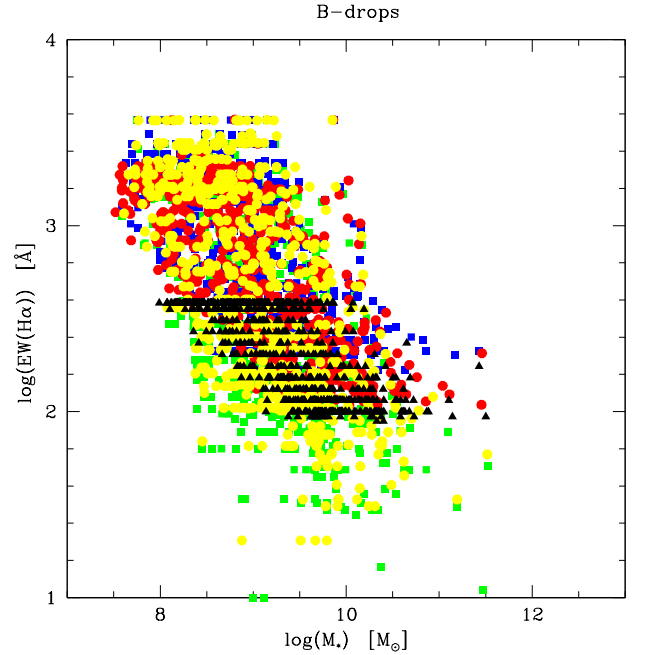


Fig. 23. Predicted (rest frame) $H\alpha$ equivalent width of the B-drop galaxies as a function of the stellar mass. Different colors indicate the different models, as in previous plots. For all SFHs an anti-correlation of $W_{H\alpha}$ with galaxy mass is expected. However, the detailed values of the equivalent width of each galaxy, and the range of $W_{H\alpha}$ covered, are model dependent.

The predicted $H\alpha$ equivalent widths cover a wide range, with a maximum reaching up to $\sim 3000 \text{ \AA}$ for some rare cases of very young galaxies. Most SFHs, except for the model with constant SFR, predict a fairly wide distribution of equivalent widths. The rising star formation histories (models C and D) predict higher median equivalent widths, since the current star formation al-

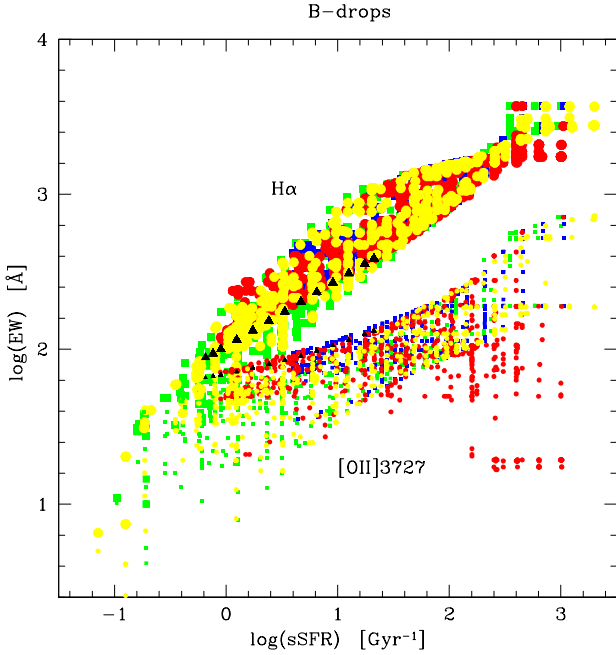


Fig. 24. Predicted correlation between the (rest-frame) equivalent width of $H\alpha$ (large symbols) and the specific star formation rate. The values shown here are derived for the sample of B-drop galaxies. However, all samples and models yield very similar relations. Small symbols show the same for $EW([O II] \lambda 3727)$, which traces less well the sSFR.

ways produces Lyman continuum photons, hence also emission lines. As expected, models with constant SFR predict a relatively narrow range of equivalent widths, limited by a minimum $W_{H\alpha} \gtrsim 100 \text{ \AA}$, which is reached close to the maximum age of $\lesssim 1$ Gyr. Only models allowing for some decline of star formation (e.g. model A, E), can predict objects with very weak or no emission lines, as clearly shown in Fig. 21 and 22. From these figures is evident that measurements of the equivalent width distribution in LBG samples can, in principle, distinguish different star formation histories. In practice, however, such line measurements are currently difficult or not yet possible, due to limited sensitivity/access at the observed near-IR wavelengths. For this task, recombination lines such as $H\alpha$ should ideally be used, as they trace directly current star formation, whereas metal lines depend more strongly on nebular conditions (metallicity etc.).

The $H\alpha$ fluxes predicted for $z \sim 4$ sample are between 10^{-18} and $10^{-16} \text{ erg s}^{-1} \text{ cm}^{-2}$, with the lowest median predicted for the SFR=const model. The predicted $[O II] \lambda 3727$ fluxes are in a similar range, but less differences are expected between different SFHs, as already mentioned above.

Not surprisingly, we find a relatively strong (anti-)correlation of the $H\alpha$ equivalent width with galaxy mass, shown in Fig. 23. Obviously different models occupy somewhat different regions of this plot, but in all cases do we find such a behavior. Indeed, this trend is expected, since the average age decreases and the specific star formation rate ($sSFR = SFR/M_*$) increases with decreasing galaxy mass for all SFHs (dBSS12). $W_{H\alpha}$ decreases also with galaxy age, but the spread in age can be very large, given various star formation timescales. The best correlation is indeed found between the $H\alpha$ equivalent width and the specific SFR, shown in Fig. 24. Again, this is a natural trend, since the $H\alpha$ equivalent width measures the ratio between the $H\alpha$ flux — tracking the current SFR — and the underlying continuum flux,

which depends on the accumulated stellar mass. We note that all models predict a very similar relation, which also holds for all samples from $z \sim 3$ to 6, although they occupy different regions of the relation. Measurements of $W_{H\alpha}$ (from spectroscopy or estimates from broad-band photometry) may therefore be used to determine the sSFR of individual high- z galaxies. As Fig. 24 also shows, metal lines such as $[O II] \lambda 3727$, which are not recombination lines, trace the sSFR less well.

Our predicted equivalent widths are comparable to those found recently in emission line galaxies at $z \sim 0.6 - 2.4$ for $[O II] \lambda 3727$, $[O III] \lambda \lambda 4959, 5007$, and $H\alpha$ (Straughn et al. 2009; Atek et al. 2011; van der Wel et al. 2011). An anti-correlation of $W_{H\alpha}$ with galaxy mass is found at all redshifts, where data is currently available, from $z = 0$ to 2–2.6, as recently discussed by Fumagalli et al. (2012). Furthermore, the predicted $H\alpha$ equivalent widths of the B-drops are in good agreement with the observations of $z \sim 2-2.6$ LBGs by Erb et al. (2006); Mancini et al. (2011) in the same mass range (typically at $M_* \gtrsim 10^{10} M_\odot$). Our models thus predict that this trend of increasing $H\alpha$ equivalent width continues down to LBGs of lower mass.

The 47 strong $H\alpha$ emitters identified by Shim et al. (2011b) at $z \sim 4$ are included in our LBG sample, and amply discussed in dBSS12. Their selection, based on an excess in the $3.6 \mu\text{m}$ filter with respect to $4.5 \mu\text{m}$, is sensitive to $EW(H\alpha) \gtrsim 200 \text{ \AA}$. Clearly, our method is able to detect/predict weaker lines, although of course with increasing uncertainty (not shown here). The highest inferred equivalent widths from Shim et al. (2011b), well in excess of 1000 \AA , are comparable to our values, as are the predicted $H\alpha$ fluxes. Although very rare at low redshift, galaxies with $EW(H\alpha) > 500 \text{ \AA}$ also exist in nearby galaxies, as pointed out by Shim & Chary (2012). They are all found at masses well below $\log M_* \lesssim 9.5 M_\odot$ and at high sSFR, quite compatible with our model predictions.

We conclude that the emission line strengths predicted by our models from fits to the observed broad-band photometry and the correlations found are compatible with the currently existing data and trends. Future observations of emission lines in $z \sim 3-6$ LBGs with existing and new ground-based facilities, and with the James Webb Space Telescope will hopefully provide further tests on the importance of emission lines and constraints on the star formation histories and specific star formation rate of these galaxies.

7. Discussion

7.1. Influence of different extinction laws

All our SED fits have been carried out using the Calzetti attenuation law, commonly thought to be appropriate for starburst galaxies. To examine the effect of other laws we have rerun all our fits for the B-drop sample with the steeper attenuation/extinction law for the SMC Prevot et al. (1984); Bouchet et al. (1985). Other laws, intermediate between the relatively grey Calzetti law and the steep SMC curve, should yield intermediate results.

Overall, we find a lower fit quality (higher reduced χ^2_ν) for the vast majority of objects using the SMC law. However, for most of them the difference remains relatively small ($\Delta\chi^2_\nu \lesssim 1$). We verified that no systematic effect is found as a function of galaxy age, as could e.g. be expected if young galaxies (e.g. $t < 100 \text{ Myr}$, as judged by the age derived assuming the Calzetti law) would be better fit with the SMC law, as suggested e.g. by Reddy et al. (2010, 2012).

Since the SMC law is steeper than that of Calzetti, SED fits for LBGs are generally yield a lower UV attenuation f_{UV}

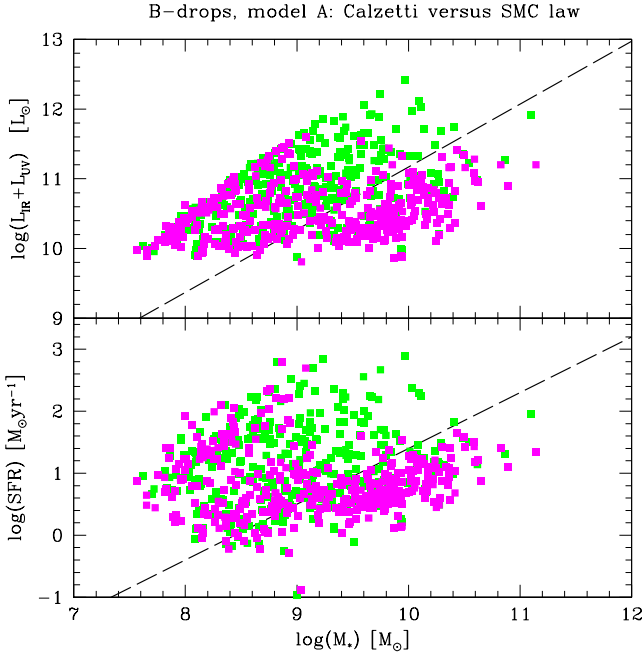


Fig. 25. Results/predictions from SED fits of the B-drop sample for model A (declining SFHs) assuming the Calzetti attenuation law (green squares) or the SMC extinction law (magenta). *Top:* IR+UV luminosity as a function of the stellar mass. *Bottom:* Current star formation rate versus stellar mass.

(and even more so a lower A_V), older ages, and hence on average somewhat larger stellar masses (e.g. Papovich et al. 2001; Verma et al. 2007; Yabe et al. 2009; Reddy et al. 2010). As expected, our fits including nebular lines also yield the same average trends. The young ages favored with the Calzetti law for some objects by the strong $H\alpha$ excess at $3.6\ \mu\text{m}$ are in part compensated by increasing the star formation timescale τ for declining SFHs. The resulting $H\alpha$ equivalent width distribution (cf. Fig. 21) remains quite similar, with the largest differences due to the assumed star formation histories.

Important differences of the SED fits with the SMC law are in particular a lower SFR and less IR emission. The former is due both to the older age (hence lower SFR/UV, cf. Fig. 2) and to the lower UV attenuation. The lower attenuation implies immediately a lower IR luminosity. For model A (declining SFHs) the median SFR of our B-drop sample is lowered by a factor ~ 2 , from 11.6 to $5.4\ M_\odot\ \text{yr}^{-1}$, the median IR luminosity from $4. \times 10^{10}\ L_\odot$ by a factor ~ 5 , compared to SED fits with the Calzetti law. The effect of adopting the SMC law on the SFR–mass on the $(L_{\text{IR}}+L_{\text{UV}})$ –mass relations for model A are shown in Fig. 25. The top panel clearly shows the reduced IR luminosity, implying a lack of B-drop galaxies with $L_{\text{IR}} \gtrsim 2. \times 10^{11}\ L_\odot$ (in this sample) if the SMC law was applicable. A large scatter is still found in the SFR–mass relation with some objects reaching large specific SFRs, as shown in the bottom panel. However, at masses $\gtrsim 10^9\ M_\odot$ the SED fits with the SMC law predict basically no LBGs with high specific SFR, i.e. above the $z \sim 2$ relation of Daddi et al. (2007). This shift to lower SFR values is again mostly due to age shifts, leading to ages $\gtrsim 100\ \text{Myr}$ for all galaxies with $M \gtrsim 10^9\ M_\odot$. It must, however, be remembered that the model SFR shown here represents the current SFR, which shows a wider dynamic range (spread) than the observable UV and IR luminosity (cf. Sect. 4.3).

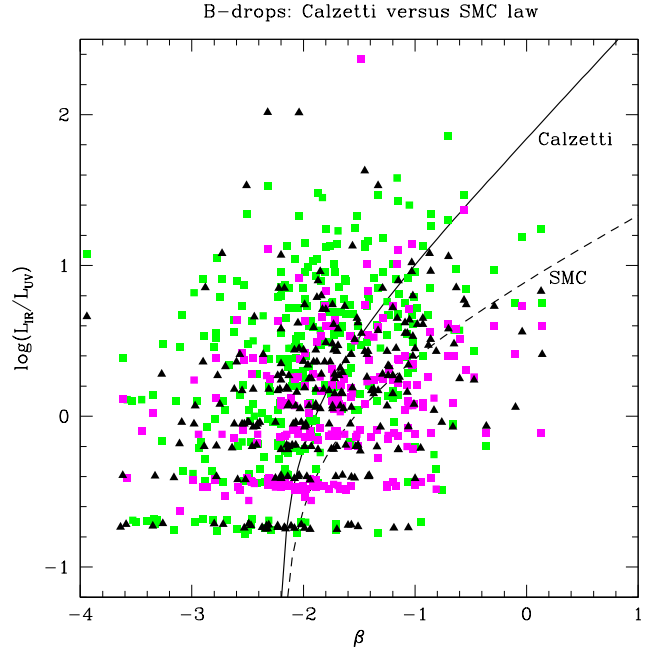


Fig. 26. Predicted IR/UV luminosity ratio as a function of the observed UV slope determined from SED fits of the B-drop sample for model A (declining SFHs) assuming the Calzetti attenuation law (green squares) or the SMC extinction law (magenta). Black triangles show the predictions for model B (constant SFR) with the Calzetti law for comparison. The solid (dashed) lines show the expected relation for galaxies with an intrinsic UV slope of $\beta \approx -2.2$ for the two attenuation laws.

At low redshift, and occasionally at $z \sim 2$ – 3 , observations of the IR/UV ratio and measurements of the UV slope β have been used to distinguish the attenuation law (e.g. Baker et al. 2001; Siana et al. 2008, 2009; Reddy et al. 2010). The so-called IRX– β plot, based on the predicted IR luminosity plus the observed L_{UV} and β , for our $z \sim 4$ LBG sample and for the two attenuation laws is shown in Fig. 26. As already mentioned above, a lower IR/UV ratio is found from SED fits using the SMC law. Besides an accurate measurement of the IR/UV ratio (soon feasible with ALMA), this method requires also a good knowledge of the intrinsic UV slope, and accurate measurements of β to constrain the attenuation law. Indeed, as clear from this plot, UV slope measurements of individual galaxies show a large scatter and their errors are relatively large since the β slope depends on one UV color, here $\beta \propto 5.3 \times (i - z)$ color, following Bouwens et al. (2009). More accurate measurements are feasible, e.g. using more photometric bands or based on SED fits (Finkelstein et al. 2011; Castellano et al. 2012). In any case, the use of the IRX– β plot to distinguish attenuation laws also requires the knowledge of the intrinsic UV slope, which may not be unique, since a priori dependent on the star formation history, age, and metallicity of the stellar population.

Distinguishing different attenuation laws may thus not be straightforward. However, some combinations of star formation history and attenuation law are clearly distinguishable once IR luminosities are measured with ALMA. As already mentioned, our SED fits to the present data yield in general better fits with the Calzetti law for the vast majority of objects, although the difference in χ^2_ν is not very large.

7.2. Comparison with earlier studies

We shall now briefly discuss other papers, which have presented tests for or constraints on different star formation histories for Lyman break galaxies using also the IR as a constraint.

To the best of our knowledge, our study is the first discussing SED fits with various star formation histories including both declining and rising parametrisations for a large number of $z \sim 3\text{--}6$ LBGs. At somewhat lower redshift Reddy et al. (2012) have recently examined a sample of ~ 300 LBGs with MIPS $24\ \mu\text{m}$ detections and spectroscopic redshifts $1.5 \leq z \leq 2.6$. The $24\ \mu\text{m}$ flux is used to infer the IR luminosity, which in turn provides an independent constraint on the SFR and dust content (as discussed above and in earlier papers, cf. Reddy et al. 2008). From their work Reddy et al. (2012) conclude that rising star formation histories provide a better agreement between different SFR indicators, and hence that declining star formation histories may not be accurate for typical galaxies at $z \gtrsim 2$.

Obviously, this conclusion is in contrast to ours, since we find that declining SFHs provide the best fits for the majority of $z \sim 3\text{--}6$ LBGs, and that delayed and rising star formation histories fare comparably. How can we understand these differences? In their comparison of star formation rates Reddy et al. (2012) find two different behaviors. First, for galaxies classified as “young” ($t < 100$ Myr) according to their SED fits with the Calzetti law, they find that the SFR inferred from the fits, SFR(SED), is systematically larger than the SFR(IR+UV) derived from the UV and IR luminosity using the standard calibrations of Kennicutt (1998). From this they conclude that there is an apparent conflict with young ages, which they propose to resolve by invoking a different, steeper attenuation law for young objects. We question the solidity of such a conflict, and argue that their resolution is by no means unique. Indeed, although they note that a young age is not compatible with assumptions made for the standard UV–SFR conversion, they neglect the fact that both IR and UV conversions depend on the SFH and age in a similar way (see their Fig. 25 and Fig. 2), modifying the (UV+IR)—SFR conversion upward by typically twice the amount they state. The effect they find is clearly shown to predicted for our $z \sim 4$ sample, as illustrated in Fig. 15, where we note that for the majority of objects fitted with unconstrained ages and found to be younger than 100 Myr from our models, the SFR(SED) is larger than the SFR(IR+UV) obtained from an inconsistent application of the standard calibrations. A consistent analysis of the time and star formation history dependent UV and IR emission may therefore also simply explain the apparent problem pointed out by Reddy et al. (2012) for young galaxies without resort to an age dependent attenuation law.

The second different behavior noted by Reddy et al. (2012) is for galaxies classified by their model as being older than 100 Myr. For these they find that exponentially declining SFHs yield SFR(SED) systematically lower than SFR(IR+UV), from which they conclude that such histories are disfavored. Indeed, their models apparently yield best-fit solutions with $t/\tau \gg 1$ for these galaxies, which naturally explains the discrepancy between these SFR indicators (cf. Reddy et al. 2012, and Fig. 2). However, UV continuum observations, showing clear signatures of young massive stars, and $H\alpha$ measurements for some of the LBGs indicate $t/\tau < 1$ according to Reddy et al. (2012). From this, the authors conclude that exponentially declining SFHs are statistically inconsistent with the observations. We cannot verify the results of Reddy et al. (2012) as their observational data is not published. However, we note that age is the most model dependent quantity and that systematically younger ages are obtained when

nebular emission is taken into account (cf. above and dBSS12). Furthermore in our analysis of $z \sim 3\text{--}6$ LBGs we find values of $t/\tau < 1$ for the majority of objects, in agreement with the observational arguments mentioned by Reddy et al. (2012). We may thus suspect that a reanalysis of $z \sim 2$ LBGs with models including nebular emission may yield different results.

In short, we find that the conclusion of Reddy et al. (2012) favoring clearly rising star formation histories over declining ones for $z \sim 2$ LBGs is not robust. In any case, stellar populations/SFHs of LBGs at higher redshift may be different, and from the result of Reddy et al. (2012) at $z \sim 1.6\text{--}2.4$ one cannot conclude that exponentially declining SF histories are not appropriate for LBGs at $z \geq 3$. It is therefore important to obtain direct measurements of the IR luminosity at higher redshifts.

Other comparisons with Reddy et al. (2012) regarding constant and rising star formation histories have already been discussed in dBSS12, and shall not be repeated here.

7.3. Possible caveats

Before closing this section, we wish to remind the reader that our SED fitting tool suffers from the same possible limitations as other models, including e.g. the unknown star formation histories of galaxies (modeled here with simple parametrisation), the question of multiple populations and the “outshining” problem due to young populations, uncertainties related to the extinction (which law? a unique attenuation for all stars? etc.), uncertainties in the stellar initial mass function, and of course also uncertainties in stellar evolution and atmosphere models. Some of these issues are e.g. addressed by Maraston et al. (2010); Wuyts et al. (2009); Charlot & Longhetti (2001); Walcher et al. (2011); Levesque et al. (2012); Schaerer (2012).

In this respect our results should of course be considered as “differential”, i.e. with respect to other models making the same/similar assumptions, but neglecting the effects of nebular emission and of variable star formation histories, which are explored here systematically for the first time for a large sample of Lyman break galaxies. Concerning nebular emission our models make some simple assumptions, which may also influence the results. Our main assumptions are no loss of ionizing photons (i.e. no Lyman continuum escape, no dust inside the HII regions etc.), and the same attenuation for the stellar continuum and nebular lines. Both assumptions maximize to some extent the possible contribution of nebular emission, and could therefore lead to an overestimate of the effects of nebular emission on the derived physical parameters. The results would then be intermediate between the present case with nebular emission and the models without, discussed in depth in dBSS12. Exploring variations of the above assumptions may be interesting and worth pursuing in future studies. In any case, it is clear that for a majority (approximately two thirds) of LBGs the inclusion of nebular effects improves the quality of the SED fits, and that models without nebular lines cannot reproduce the observed excess in certain photometric bands (most prominently the $3.6\ \mu\text{m}$ excess for galaxies with redshift between 3.8 and 5). For the bulk of the LBGs our models should therefore provide a better description than previous models neglecting nebular emission, despite the simplifying assumptions made. To progress further on these questions additional observational constraints, such as direct measurements of IR luminosities, medium-or narrow-band photometry, or measurements of emission lines should be of considerable help. The predictions presented here should also provide a useful base for future comparisons and tests of the SED models.

8. Summary and conclusions

Following up on our earlier detailed study (de Barros et al. 2012) of a large sample of LBGs from redshift $z \sim 3$ to 6 located in the GOODS-South field, using for the first time an SED fitting tool including the effects of nebular emission on the synthetic photometry, we have examined the impact of different star formation histories (SFHs) on the derived physical parameters of these galaxies, on the SFR–mass relation, on different SFR indicators (UV and IR), on the expected dust extinction and the corresponding IR luminosity, and on the expected strengths of emission lines such as H α and [O II] $\lambda 3727$.

To do so, we have carried out SED fits for five different SFHs including exponentially rising and so-called delayed SFHs, plus the three histories already considered in dBSS12 (see Table 1 and Fig. 1). Metallicity is also treated as a free parameter, and we have examined the effect of two different extinction/attenuation laws (Calzetti and SMC). The usual physical parameters, stellar mass, SFR, age, and attenuation are derived from the SED fits to the broad band photometry reaching from the U band to 8 μm , using Monte Carlo simulations to derive their median values (and the detailed probability distribution function, generally not discussed here). We have also computed consistently the predicted IR luminosities, L_{IR} , for all galaxies, assuming energy-conservation, i.e. that all the radiation absorbed by dust is reemitted in the IR. Finally, the predicted IR luminosities have been translated to flux predictions in various IR bands, assuming modified black body spectra. The L_{IR} predictions allow us in particular to examine in a consistent way the effects of variable SFHs and ages on this observable quantity, showing thus significant departures from results assuming inconsistent SFR(IR) or SFR(UV) calibrations.

Our main results concerning the impact of star formation histories on the physical parameters of LBGs, exemplified to a sample of 705 LBGs at $z \sim 4$ (B-drop galaxies), can be summarized as follows (see Sect. 3):

- Compared to commonly adopted SED fits assuming constant SFR, no nebular emission and an age prior of $t > 50$ Myr, models with exponentially declining SFHs, nebular lines and no age constraint yield younger ages, lower stellar masses, higher current SFR, higher specific star formation rates ($\text{sSFR} = \text{SFR}/M_*$), and higher dust extinction (A_V), as already shown in de Barros et al. (2012).
- Exponentially declining SFHs yield overall the best fits for the majority of LBGs.
- Assuming delayed star formation histories one obtains basically identical physical parameters (and fit qualities) as for exponentially declining SFHs.
- Rising star formation histories with variable timescales imply generally a similar stellar masses, and comparable or somewhat higher dust extinction than models assuming declining SFHs. The latter leads to the highest star formation rates and to similar or higher IR luminosities as for declining histories.
- Overall “standard” models assuming constant and neglecting lines predict systematically higher stellar masses, lower extinction, lower SFR, lower IR luminosities, and more narrow range of equivalent widths for optical emission lines than all the other star formation histories considered here.

Combining these different physical parameters we obtain the following (Sect. 4):

- We find significant deviations between the derived SFR and IR luminosity from the commonly used SFR(IR) or

SFR(IR+UV) calibration of Kennicutt (1998). Such differences naturally arise, due to differences in the derived ages and in the adopted star formation histories. In most cases (i.e. for most galaxies and SFHs) we find that the Kennicutt relation will underestimate the true, current SFR derived from the SED fits (Sect. 4.2). Consistent SED studies including also the IR are therefore necessary, if the SFHs and ages may differ from those assumed in standard SFR calibrations.

- A large scatter is found in the SFR–mass relation for models with declining and delayed SFH and no age prior (cf. de Barros et al. 2012). The same also hold for models with rising star formation histories. The scatter is reduced when a minimum age (e.g. $t > 50$ Myr) is adopted. Even in this case, models with rising SFHs can show a large scatter, since high SFRs are found to the high(er) extinction.
- A large scatter in the SFR–mass relation does not necessarily imply the same scatter in the L_{IR} (or $(L_{\text{IR}} + L_{\text{UV}})$ –mass relation and vice versa, when the IR luminosity is computed consistently from the chosen SED model (i.e. accounting for age and SFH effects). The same also applies to SFR(UV)–mass diagrams where the UV luminosity and the corresponding standard SFR conversion is used. We suggest that the true scatter in the SFR–mass relation obtained in this way may indeed be underestimated, if the true star formation histories are variable on relatively short timescales. Indeed such SFH variations can reproduce more successfully features related to emission lines, such as the observed 3.6 μm excess in $z \sim 4$ –5 LBGs. They may also be more relevant to at higher redshift, where the dynamical timescales decrease with $(1+z)^{-3/2}$.

Our consistent predictions of IR luminosities (and fluxes) show that different SFHs lead to significantly different amounts of reddening and hence to different IR/UV luminosity ratios. Measurements of IR luminosities of individual LBGs or statistical samples of such galaxies can be used to distinguish different SFHs, and hence also different specific SFRs predicted by such models. ALMA observations will thus be able to provide independent constraints on behavior of the sSFR at high redshift, and on the scatter in the SFR–mass relation.

We show predictions for the IR luminosities of B-drop and i-drop galaxies for different star formation histories and as a function of UV magnitude. The typical/median L_{IR} is predicted to be $L_{\text{IR}} \sim 10^{10...11} L_{\odot}$ for LBGs with absolute UV magnitudes of $M_{\text{UV}} \sim -22$ to -19 .

Finally we also show the predicted strengths (equivalent widths) of the H α and [O II] $\lambda 3727$ emission lines. Again, different star formation histories naturally lead to different EW distributions, which can in principle be used to constrain the SFHs. Our models predict on average higher equivalent widths in low mass galaxies, in agreement with currently available observations at $z < 3$, and a clear anti-correlation of $W_{\text{H}\alpha}$ with the specific SFR.

Our predictions should in particular provide new tests using IR observations with ALMA and/or measurements of (rest-frame) optical emission lines to obtain a better insight on the star formation histories of high redshift LBGs, on the behaviour of the SFR–mass relations and on the evolution of the specific SFR with redshift.

Acknowledgements. We thank Mirka Dessauges-Zavadsky, Thomas Greve, and Michel Zamojski, for discussions and comments on the manuscript, and numerous other colleagues for stimulating and critical discussions during the last two years. This work is supported by the Swiss National Science Foundation.

References

- Atek, H., Siana, B., Scarlata, C., et al. 2011, *ApJ*, 743, 121
- Baker, A. J., Lutz, D., Genzel, R., Tacconi, L. J., & Lehnert, M. D. 2001, *A&A*, 372, L37
- Bolzonella, M., Miralles, J., & Pelló, R. 2000, *A&A*, 363, 476
- Boquien, M., Buat, V., Boselli, A., et al. 2012, *A&A*, 539, A145
- Bouché, N., Dekel, A., Genzel, R., et al. 2010, *ApJ*, 718, 1001
- Bouchet, P., Lequeux, J., Maurice, E., Prevot, L., & Prevot-Burnichon, M. L. 1985, *A&A*, 149, 330
- Bouwens, R. J., Illingworth, G. D., Franx, M., et al. 2009, *ApJ*, 705, 936
- Bouwens, R. J., Illingworth, G. D., Oesch, P. A., et al. 2011, *ArXiv e-prints*
- Bruzual, G. & Charlot, S. 2003, *MNRAS*, 344, 1000
- Buat, V., Iglesias-Páramo, J., Seibert, M., et al. 2005, *ApJL*, 619, L51
- Burgarella, D., Buat, V., & Iglesias-Páramo, J. 2005, *MNRAS*, 360, 1413
- Calzetti, D., Armus, L., Bohlin, R. C., et al. 2000, *ApJ*, 533, 682
- Castellano, M., Fontana, A., Grazian, A., et al. 2012, *A&A*, 540, A39
- Charlot, S. & Longhetti, M. 2001, *MNRAS*, 323, 887
- da Cunha, E., Charlot, S., & Elbaz, D. 2008, *MNRAS*, 388, 1595
- Daddi, E., Dickinson, M., Morrison, G., et al. 2007, *ApJ*, 670, 156
- Davé, R., Oppenheimer, B. D., & Finlator, K. 2011, *MNRAS*, 415, 11
- de Barros, S., Schaerer, D., & Stark, D. 2012, *ArXiv e-prints* (dBSS12)
- de Barros, S., Schaerer, D., & Stark, D. P. 2011, *ArXiv e-prints*
- Dutton, A. A., van den Bosch, F. C., & Dekel, A. 2010, *MNRAS*, 405, 1690
- Egami, E., Kneib, J.-P., Rieke, G. H., et al. 2005, *ApJL*, 618, L5
- Elbaz, D., Daddi, E., Le Borgne, D., et al. 2007, *A&A*, 468, 33
- Erb, D. K., Shapley, A. E., Pettini, M., et al. 2006, *ApJ*, 644, 813
- Eyles, L. P., Bunker, A. J., Stanway, E. R., et al. 2005, *MNRAS*, 364, 443
- Finkelstein, S. L., Papovich, C., Giavalisco, M., et al. 2010, *ApJ*, 719, 1250
- Finkelstein, S. L., Papovich, C., Salmon, B., et al. 2011, *ArXiv e-prints*
- Finlator, K., Davé, R., & Oppenheimer, B. D. 2007, *MNRAS*, 376, 1861
- Finlator, K., Oppenheimer, B. D., & Davé, R. 2010, *MNRAS*, 1532
- Finlator, K., Oppenheimer, B. D., & Davé, R. 2011, *MNRAS*, 410, 1703
- Fumagalli, M., Patel, S., Franx, M., et al. 2012, *ArXiv e-prints*
- González, J. E., Lacey, C. G., Baugh, C. M., Frenk, C. S., & Benson, A. J. 2012, *MNRAS*, 3152
- González, V., Labbé, I., Bouwens, R. J., et al. 2011, *ApJL*, 735, L34+
- Iglesias-Páramo, J., Buat, V., Hernández-Fernández, J., et al. 2007, *ApJ*, 670, 279
- Kennicutt, Jr., R. C. 1998, *ARA&A*, 36, 189
- Khochfar, S. & Silk, J. 2011, *MNRAS*, 410, L42
- Krumholz, M. R. & Dekel, A. 2012, *ApJ*, 753, 16
- Labbé, I., González, V., Bouwens, R. J., et al. 2010, *ApJL*, 716, L103
- Lee, S.-K., Ferguson, H. C., Somerville, R. S., Wiklind, T., & Giavalisco, M. 2010, *ApJ*, 725, 1644
- Levesque, E. M., Leitherer, C., Ekstrom, S., Meynet, G., & Schaerer, D. 2012, *ApJ*, 751, 67
- Madau, P. 1995, *ApJ*, 441, 18
- Mancini, C., Förster Schreiber, N. M., Renzini, A., et al. 2011, *ApJ*, 743, 86
- Maraston, C., Pforr, J., Renzini, A., et al. 2010, *MNRAS*, 407, 830
- McLure, R. J., Dunlop, J. S., de Ravel, L., et al. 2011, *MNRAS*, 418, 2074
- Meurer, G. R., Heckman, T. M., & Calzetti, D. 1999, *ApJ*, 521, 64
- Noeske, K. G., Weiner, B. J., Faber, S. M., et al. 2007, *ApJL*, 660, L43
- Noll, S., Burgarella, D., Giovannoli, E., et al. 2009, *A&A*, 507, 1793
- Nonino, M., Dickinson, M., Rosati, P., et al. 2009, *ApJS*, 183, 244
- Papovich, C., Dickinson, M., & Ferguson, H. C. 2001, *ApJ*, 559, 620
- Papovich, C., Finkelstein, S. L., Ferguson, H. C., Lotz, J. M., & Giavalisco, M. 2011, *MNRAS*, 412, 1123
- Prevot, M. L., Lequeux, J., Prevot, L., Maurice, E., & Rocca-Volmerange, B. 1984, *A&A*, 132, 389
- Reddy, N. A., Erb, D. K., Pettini, M., Steidel, C. C., & Shapley, A. E. 2010, *ApJ*, 712, 1070
- Reddy, N. A., Pettini, M., Steidel, C. C., et al. 2012, *ArXiv e-prints*
- Reddy, N. A., Steidel, C. C., Pettini, M., et al. 2008, *ApJS*, 175, 48
- Renzini, A. 2009, *MNRAS*, 398, L58
- Rodighiero, G., Daddi, E., Baronchelli, I., et al. 2011, *ApJL*, 739, L40
- Santini, P., Fontana, A., Grazian, A., et al. 2009, *A&A*, 504, 751
- Schaerer, D. 2012, *ArXiv e-prints*
- Schaerer, D. & de Barros, S. 2009, *A&A*, 502, 423
- Schaerer, D. & de Barros, S. 2010, *A&A*, 515, A73+
- Schaerer, D. & de Barros, S. 2011, *ArXiv e-prints*
- Schaerer, D. & Pelló, R. 2005, *MNRAS*, 362, 1054
- Shim, H. & Chary, R.-R. 2012, *ArXiv e-prints*
- Shim, H., Chary, R.-R., Dickinson, M., et al. 2011a, *ApJ*, 738, 69
- Shim, H., Chary, R.-R., Dickinson, M., et al. 2011b, *ApJ*, 738, 69
- Siana, B., Smail, I., Swinbank, A. M., et al. 2009, *ApJ*, 698, 1273
- Siana, B., Teplitz, H. I., Chary, R.-R., Colbert, J., & Frayer, D. T. 2008, *ApJ*, 689, 59
- Stark, D. P., Ellis, R. S., Bunker, A., et al. 2009, *ApJ*, 697, 1493
- Straughn, A. N., Pirzkal, N., Meurer, G. R., et al. 2009, *AJ*, 138, 1022
- van der Wel, A., Straughn, A. N., Rix, H.-W., et al. 2011, *ApJ*, 742, 111
- Verma, A., Lehnert, M. D., Förster Schreiber, N. M., Bremer, M. N., & Douglas, L. 2007, *MNRAS*, 377, 1024
- Walcher, J., Groves, B., Budavári, T., & Dale, D. 2011, *Ap&SS*, 331, 1
- Weinmann, S. M., Neistein, E., & Dekel, A. 2011, *MNRAS*, 417, 2737
- Wuyts, S., Förster Schreiber, N. M., Lutz, D., et al. 2011, *ApJ*, 738, 106
- Wuyts, S., Franx, M., Cox, T. J., et al. 2009, *ApJ*, 696, 348
- Wyithe, J. S. B. & Loeb, A. 2011, *MNRAS*, 413, L38
- Yabe, K., Ohta, K., Iwata, I., et al. 2009, *ApJ*, 693, 507